

NETWORK DYNAMICS

Cytoskeletal actin dynamics shape a ramifying actin network underpinning immunological synapse formation

Marco Fritzsche,^{1,*†} Ricardo A. Fernandes,^{1,2†} Veronica T. Chang,^{1,3} Huw Colin-York,¹ Mathias P. Clausen,^{1,4} James H. Felce,¹ Silvia Galiani,¹ Christoph Erlenkämper,⁵ Ana M. Santos,¹ John M. Heddleston,⁶ Isabela Pedroza-Pacheco,⁷ Dominic Waithe,⁸ Jorge Bernardino de la Serna,^{1,8,9,10} B. Christoffer Lagerholm,⁸ Tsung-li Liu,^{6,11} Teng-Leong Chew,⁶ Eric Betzig,⁶ Simon J. Davis,¹ Christian Eggeling^{1,8*}

Copyright © 2017
The Authors, some
rights reserved;
exclusive licensee
American Association
for the Advancement
of Science. No claim to
original U.S. Government
Works. Distributed
under a Creative
Commons Attribution
NonCommercial
License 4.0 (CC BY-NC).

T cell activation and especially trafficking of T cell receptor microclusters during immunological synapse formation are widely thought to rely on cytoskeletal remodeling. However, important details on the involvement of actin in the latter transport processes are missing. Using a suite of advanced optical microscopes to analyze resting and activated T cells, we show that, following contact formation with activating surfaces, these cells sequentially rearrange their cortical actin across the entire cell, creating a previously unreported ramifying actin network above the immunological synapse. This network shows all the characteristics of an inward-growing transportation network and its dynamics correlating with T cell receptor rearrangements. This actin reorganization is accompanied by an increase in the nanoscale actin meshwork size and the dynamic adjustment of the turnover times and filament lengths of two differently sized filamentous actin populations, wherein formin-mediated long actin filaments support a very flat and stiff contact at the immunological synapse interface. The initiation of immunological synapse formation, as highlighted by calcium release, requires markedly little contact with activating surfaces and no cytoskeletal rearrangements. Our work suggests that incipient signaling in T cells initiates global cytoskeletal rearrangements across the whole cell, including a stiffening process for possibly mechanically supporting contact formation at the immunological synapse interface as well as a central ramified transportation network apparently directed at the consolidation of the contact and the delivery of effector functions.

INTRODUCTION

T cells are activated by the binding of T cell receptors (TCRs) to antigen-loaded peptide major histocompatibility complexes on antigen-presenting cells (APCs), resulting first in the formation of TCR “microclusters” and then in their coalescence in the immunological synapse (IS), which allows the delivery of effector functions. However, signaling events, such as trafficking of TCR microclusters, must be coordinated in time and space, and this trafficking was generally expected to rely on active cytoskeletal rearrangements at each stage (1–11). Actin cytoskeletal rearrangements regulating the membrane architecture of T cells are important during initial cell-cell interactions through the formation of actin-rich protrusions, such as actin ruffles (3, 12). These, in turn, would allow the formation of “close contacts”

between T cells and APCs, favoring the transient interactions of proteins required for signaling. However, thus far, observable cytoskeletal rearrangements have mostly been limited to macroscopic changes at the basal membrane, mainly involving the formation of the actin-rich peripheral lamellipodium and an almost actin-depleted central region at the IS. It has been shown that the lamellipodium spreads and undulates at contact interfaces with activating supported lipid bilayers or glass surfaces, where it is thought to generate mechanical force in the direction of the interface center, implicating the involvement of the lamellipodium in the translocation of microclusters toward the center of the IS (13). Colocalization of actin with TCR and other proteins, such as linker of activated T cells (LAT), has been indicated at the early lamellar contacts of a spreading T cell (14). On the other hand, biochemical studies have revealed critical roles for Rho or Rac 1 guanosine triphosphatases in the control of actin assembly during signaling in T cells downstream of TCR and costimulatory receptor CD28 triggering (1, 5, 6). Experiments have suggested that GRB2-related adapter protein 2 (Gads) and SLP-76 bound to LAT might nucleate actin polymerization (14, 15). Formin proteins, which associate with the fast-growing barbed end of actin filaments and thus result in their extension, have also been implicated in the formation of IS architecture (5, 16), whereas the Wiskott-Aldrich syndrome protein (WASP), which supports branching of short actin filaments, has been implicated in the stabilization of the IS (17). The direct involvement of the actin cytoskeleton in T cell responses has otherwise only been inferred from the effects of pharmacological or genetic disruption, which are generally found to impair T cell activation and to lead to severe T cell dysfunction (10). Moreover, there have been efforts to understand the relationship of directed

¹MRC Human Immunology Unit, Weatherall Institute of Molecular Medicine, University of Oxford, Headley Way, Oxford OX3 9DS, UK. ²Department of Molecular and Cellular Physiology, Stanford University School of Medicine, Stanford, CA 94305, USA. ³Division of Structural Biology, Wellcome Trust Centre for Human Genetics, University of Oxford, Oxford OX3 7BN, UK. ⁴Center for Biomembrane Physics (MEMPHYS), University of Southern Denmark, Campusvej 55, DK-5230 Odense M, Denmark. ⁵Institut Curie, 26 rue d'Ulm, 75248 Paris cedex 05, France. ⁶Janelia Research Campus, Howard Hughes Medical Institute, 19700 Helix Drive, Ashburn, VA 20147, USA. ⁷Nuffield Department of Medicine, University of Oxford, Oxford OX3 7FZ, UK. ⁸Wolfson Imaging Centre, Weatherall Institute of Molecular Medicine, University of Oxford, Headley Way, Oxford OX3 9DS, UK. ⁹Central Laser Facility, Rutherford Appleton Laboratory, Research Complex at Harwell, Science and Technology Facilities Council, Harwell-Oxford Campus, Didcot OX11 0FA, UK. ¹⁰Department of Physics, King's College London, London WC2R 2LS, UK. ¹¹Vertex Pharmaceuticals, 11010 Torreyana Road, San Diego, CA 92121, USA.

*Corresponding author. Email: marco.fritzsche@rdm.ox.ac.uk (M.F.); christian.eggeling@rdm.ox.ac.uk (C.E.)

†These authors contributed equally to this work.

TCR microcluster mobility and actin turnover by pharmacologically disrupting filamentous actin (F-actin) flow (10). These interventions arrest microcluster translocation and block sustained calcium signaling detected during lamellipodial undulations in Fura-2-loaded T cells (10). Overall, these experiments have highlighted the importance of functional actin polymerization dynamics for successful IS formation, but the detailed contributions of the cytoskeleton to signaling have yet to be unraveled.

Unraveling the complex contribution of the actin cytoskeleton requires full understanding of its structural characteristics. The actin cytoskeleton of eukaryotes forms four distinct structures: the actin cortex, contractile rings, lamellipodia, and actin-rich protrusions (18–20). These allow the actin network, assisted by myosin-II proteins, to transduce chemical signals into mechanical force. In turn, the interplay between all of these factors facilitates reorganization and adjustment of F-actin networks in response to environmental cues (18). The actin cortex is probably the most important actin structure underlying the cell membrane of eukaryotic cells, and it comprises polydisperse actin filaments undergoing constant turnover (21, 22). These actin dynamics involve either (i) formin proteins, which associate with the fast-growing barbed end of long actin filaments, resulting in their extension, or (ii) the Arp2/3 complex, which is a nucleator of the branching of short actin filaments that is activated by WASp (22). Through a dynamic interplay with myosin-II minifilaments, the cortical network provides the cell with mechanical and structural integrity and drives shape changes (23). Contractile actin rings serve to pinch and separate daughter cells during cell division (24). The lamellipodium, which is connected to the actin cortex by its lamellum, is a flat, highly dynamic structure composed of mostly Arp2/3-nucleated actin filaments and a few structurally stabilizing, long formin-mediated filaments (25). Furthermore, ramified actin networks underneath the central membrane region of cellular interfaces have been described and suggested to assist molecular transport, hence termed transportation networks (26).

Part of the reason for the limited progress in understanding the role of cytoskeleton in lymphocyte function, which lags well behind that for, for example, fibroblasts (27–29), is that previous studies of actin dynamics in T cells have, for the most part, relied on conventional resolution optical imaging, most commonly of the aforementioned basal macroscopic arrangements of the lamellipodium using total internal reflection fluorescence (TIRF) microscopy. This has meant that little is known about the actin cytoskeleton in non-contacting or resting T cells, and it has precluded the detailed analysis of the three-dimensional (3D) microscopic organization of actin across the whole of the T cell and not only at the basal membrane. This has led to the paradoxical finding that no distinct actin network has been detected below the IS (10, 30, 31), although it is hypothesized that this network could drive microcluster formation and translocation and, therefore, IS formation (2, 10, 13). For example, trafficking of TCR microclusters is thought to be achieved by the combination of centripetal actin flow of the lamellipodium and coordinated contractions of actin arcs rich in myosin-II located at the rear of the lamellipodium (2, 11, 32–35). Yet, important details of the involvement of the actin cytoskeleton in T cell activation remain unclear: (i) Although the lamellipodial actin flow and localization of myosin-II motors at the basal plane of the lamellipodium have been previously described in detail (10, 17, 33, 36–38), their global 3D organization across the whole cell is largely unknown. (ii) The nanoscale organization of actin networks, including meshwork

sizes, F-actin turnover, and lengths of actin at each stage of T cell activation, remains uncharacterized. (iii) Transportation networks have not been reported in T cells to date, although these networks are generally believed to be connected to molecular transport (26). (iv) The relevance of the actin cytoskeleton for early TCR signaling and, thus, the initiation of IS formation, for example, of calcium release, are poorly understood (39).

Here, we use a range of advanced fluorescence microscopy tools, including super-resolution stimulated emission depletion (STED) microscopy and lattice light-sheet microscopy (LLSM), on resting and surface-activated Jurkat T cells to show that, in the course of their activation, the actin cytoskeleton of T cells undergoes a series of macroscopic and microscopic transformations rivaling the complexity of those accompanying eukaryotic cell division. These transformations involve (i) global reorganization across the whole cell, including the formation of each of the four main actin structures (cortex, ring, lamellipod, and spikes); (ii) the occurrence of a distinct inward-growing ramifying transportation network of actin below the IS, whose dynamics are correlated with TCR rearrangements; and (iii) distinct changes in the actin filament lengths and meshwork sizes, suggesting that a high degree of cytoskeletal plasticity allows T cells to form cellular contacts at different length and time scales and creating a very flat and particularly stiff contact. Finally, we reexamine whether actin also contributes to the very earliest signaling events leading to initial calcium responses and unexpectedly find that early T cell signaling per se both preempts and proceeds independently of actin remodeling and spreading.

RESULTS

Experimental conditions

Modified glass surfaces are widely used to study the earliest stages of T cell activation (2, 13, 15, 40–42). To directly compare results for contact formation with and without stimulation, we chose the well-established systems of Jurkat T cells and coating microscope cover glass with anti-CD3 and anti-CD28 antibodies (9, 43). To encourage T cells to adhere to the glass surface, coverslips were blocked with 10% fetal calf serum (FCS) before experimentation, facilitating integrin-mediated attachment. Furthermore, to ensure full activation, we pre-coated the glass surfaces with donkey anti-mouse immunoglobulin G (IgG) in addition to the high-off rate ($k_{\text{off}} = 0.39 \text{ s}^{-1}$) anti-CD3 antibody OKT3 at 10 $\mu\text{g/ml}$ and anti-CD28 antibodies (see Materials and Methods) (41, 42). This contrasts with some studies in which activating antibodies with unphysiologically low dissociation rates were used (that is, the high-affinity UCHT1 anti-CD3 antibody with $k_{\text{off}} = 0.011 \text{ s}^{-1}$) (2, 13, 15, 40). We also performed control experiments with T cells contacting unspecific IgG-coated [that is, nonfunctionalized (or non-activating)] glass surfaces and cells suspended in hydrogel to study “resting” behavior (see Materials and Methods).

Novel F-actin structures and mesh sizes form in response to activation signals

We initially performed 3D super-resolution STED microscopy experiments ($\sim 60 \text{ nm}$ laterally and down to $\sim 300 \text{ nm}$ axially; fig. S1) to investigate the actin cytoskeleton in live and fixed Jurkat T cells (expressing LifeAct-citrine or labeled with Alexa Fluor 488-phalloidin, respectively). From these experiments, we produced stacks of images of the actin cytoskeleton taken at different axial positions. This allowed 3D reconstructions of the actin cortex and the intracellular cytoplasmic

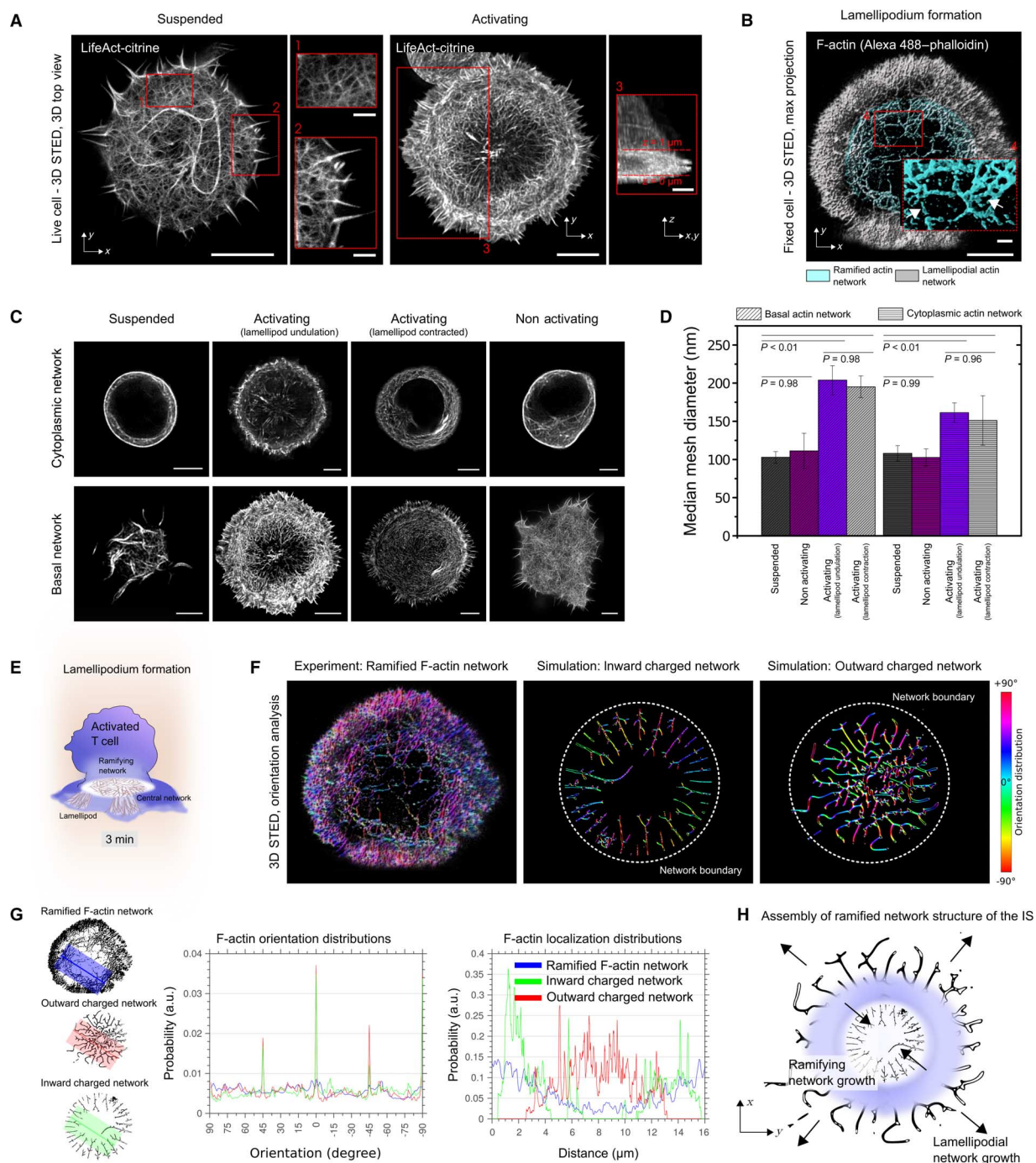


Fig. 1. Super-resolution 3D STED microscopy of the actin cortex in Jurkat T cells. (A) Top view of representative 3D reconstruction of the cell cortex (LifeAct-citrine); overview images (x-y projections) and close-ups of regions marked by the red boxes (insets: x-y projections in the left panel and x-y-z display in the right panel) of a suspended (left) and activated T cell (right). Scale bars, 5 μm (main figures) and 1 μm (insets). (B) Representative 3D STED image of Alexa Fluor 488-phalloidin-labeled F-actin: Maximum projections of the z-stacks between $z = 0 \mu\text{m}$ (glass surface) and $z = 1 \mu\text{m}$ confirm the rosette-like actin network comprising a lamellipodial network at $z = 0 \mu\text{m}$ (gray) and the additional coarser actin network at $z = 150$ to 300 nm [blue; inset: close-up of a region marked by the red box showing details of the ramification including the decreasing F-actin concentration toward the center of the network (white arrows)]. Scale bars, 100 nm. (C and D) Representative STED images and corresponding quantifications of the actin mesh size of the cortical and cytoplasmic actin networks. Scale bars, 5 μm . (E) Sketch of the ramified actin network after lamellipodium formation. (F) Representative spatial orientation map of actin filaments (color scale highlighting orientation of F-actin arms in space from light blue horizontal to red vertical, -90° to 90°) observed in the 3D STED microscopy image of (B) (left) and from simulations mimicking an inward-growing (middle) and outward-growing (right) transportation network. (G) F-actin orientation and density analysis. Left: Outline of the actin filaments identified from the experimental (upper) and simulated (middle: inward-growing network; lower: outward-growing network) data of (F). Middle: Probability of observing a certain orientation (angle relative to horizontal line) within the areas marked in the left panels. Right: Density of actin filaments along the line drawn in the right panels. a.u., arbitrary units. (H) Sketch of the actin rearrangements in T cells during IS formation.

actin network (Fig. 1A). The 3D reconstructions disclosed novel distinct filamentous structures of the actin cortex of T cells. In suspended T cells, we were able to distinguish between the cortical network beneath the cell surface and the ruffle-forming actin at the cell perimeter [45 of 45 investigated resting T cells; Fig. 1A (left, insets 1 and 2)]. T cells contacting the activating surface spread out and formed a dense cortical network forming a rosette-shaped actin structure at the leading edge of the interface, the basal lamellipodium [65 of 65 investigated activated T cells; Fig. 1, A (right, inset) and B (outer ring)], as it has been observed before (13). However, our imaging revealed a second highly ramified actin network at axial positions $z = 150$ to 300 nm above the glass contact [62 of 65 investigated activated T cells; Fig. 1, A (right) and B (cyan-labeled network, maximum projection of 3D STED images), and fig. S2A], which connected to the lamellipodial network (Fig. 1E). The location of the network likely explains why this structure was not reported in previous studies, which relied on TIRF-based imaging only. At later stages of the activation process, the ramified and the lamellipodial network contracted (fig. S2B). Although the lamellipodium was still present, this contracted network exhibited a significantly denser mesh, with the actin filaments radiating toward the center of the interface (Fig. 1C). The ramified actin network was also present in human peripheral blood (PB) CD4⁺ T cells (29 of 30 investigated activating PB T cells; fig. S2, C and D), highlighting the fact that the network was not unique to Jurkat T cells. Quantification of the mesh size of the cortical actin network at the basal plane and of the cytoplasmic actin network at the equatorial plane revealed a twofold larger mesh size in Jurkat and PB CD4⁺ T cells after contact compared to suspended T cells (Fig. 1, C and D, and figs. S2 and S3). Specifically, the actin networks in suspended and nonactivated Jurkat T cells had a mean mesh size of $\sim 100 \pm 30$ nm at first contact ($P = 0.98$, $n = 425$ measurements in 15 nonactivated cells and $n = 316$ measurements in 15 suspended cells) and those in activated/contracted Jurkat T cells had a mean mesh size of $\sim 200 \pm 20$ nm ($P < 0.01$, $n = 716$ measurements in 18 cells). PB CD4⁺ T cells were, on average, threefold smaller than Jurkat T cells ($70 \mu\text{m}^2/210 \mu\text{m}^2 = 3$, ratio of basal surface areas of PB T cells and Jurkat T cells; $n = 20$ to 30 cells) and showed actin network mesh sizes at different stages of activation that are consistently three times smaller: suspended PB T cells, $\sim 30 \pm 20$ nm at first contact; $\sim 60 \pm 20$ nm during activation and contraction (Materials and Methods).

To determine whether the changes in actin organization were caused by the activating antibodies per se or were instead induced by surface contact, we compared actin reorganization after contact of the Jurkat T cells to the functionalized (activating) and nonfunctionalized (nonactivating) glass surfaces (Fig. 1C). In contrast to our observations on the functionalized surfaces, T cells interacting with the nonfunctionalized surfaces neither polarized, formed a distinct lamellipodium, nor exhibited any ramified network (125 of 125 investigated nonactivating cells; Fig. 1D).

Architecture of the ramified actin network

The architecture of the central ramifying actin structure is typical for networks assisting molecular transport (26). Dynamic formation of these transportation networks generally consists of three growth stages: (i) strand formation, (ii) boundary formation, and (iii) geometric expansion (26). Computer simulations have shown that these transportation networks can assemble by forming strands either at its outside boundary growing toward the inner space or following initiation at the inner space and growing toward its outer boundary (26).

However, to date, there has been no report of these transportation networks in T cells. To further characterize the architecture of the observed ramified network and its similarities to a transportation network, we compared the orientations and density of its actin fibers with simulated networks of inward- and outward-growing actin structures (Fig. 1F) (26). Although the fiber orientations of the ramified actin network were comparable to those of both inward and outward growing networks, the actin fiber density was qualitatively comparable only with that of the inward network (62 of 62 investigated activating T cells with such a ramified actin network present; Fig. 1G). Similar analysis of the cortical actin in resting T cells revealed purely isotropic fiber distributions and therefore did not demonstrate any ability to function as a transportation network (45 of 45 investigated resting T cells).

In the context of T cell activation, the formation of this inward transportation network entails a symmetric boundary from where actin strands originate and grow inward for the ramified network and outward for lamellipod formation (Fig. 1H). To experimentally reveal this symmetry boundary, we next investigated the general global rearrangements of the actin cytoskeleton using LLSM.

Global actin cytoskeleton rearrangements

First, we aimed at understanding the transitions between macroscopic actin cytoskeleton rearrangements. LLSM (see Materials and Methods) allows the analysis of global single-cell dynamics for long periods (>30 min) with diffraction-limited but isotropic spatial resolution (~ 300 nm) and high temporal resolution (<40 ms per slice and 1.5 s per 3D volume) (44). T cells expressing the fluorescently tagged lymphocyte-specific protein tyrosine kinase Lck as a membrane marker (tagged via the SNAP technology and the membrane-permeable SNAP-Cell 505-Star dye-ligand) were largely spherical in suspension, that is, before contact formation, with large membrane “ruffles” erupting continuously over the T cell body with an average lifetime of $t = 100 \pm 50$ s (10 of 10 investigated cells; movie S1). Following contact with the activating antibody-coated glass surface, the T cells polarized, by decreasing their height and extending their leading edge, and spread evenly. To investigate the role of the cytoskeleton in these changes, we fluorescently labeled F-actin (LifeAct-citrine or LifeAct-SNAP and SNAP-Cell 505-Star dye-ligand) and myosin-II motor proteins (myosin regulatory light chain fluorescently labeled with HaloTag and JF647 dye-ligand). Dorsal ruffling stopped upon contacting the anti-CD3- and anti-CD28-coated surface, and instead a symmetric interface at the basal surface was formed, followed by the formation, undulation, and contraction of a lamellipod (40 of 40 investigated cells; Fig. 2A and movies S2 and S3). This lamellipod was clearly separated from central actin structures (40 of 40 investigated cells; Fig. 2A, top). Previously, under conditions of high-affinity antibody (UCHT1) stimulation, the undulating phase had been observed to be more persistent (30 to 40 min) (2).

From the LLSM data, we determined the temporal dynamics of the leading cell edge (fig. S4), specifically the length of the cell perimeter and its velocity in the direction of the contact radius (Fig. 2B), which revealed that the contact area of the cell was symmetric and grew centripetally, forming a continuous interface. Upon reaching its maximum diameter, the lamellipodium underwent a period of continuous undulation, after which it retracted (40 of 40 investigated cells; Fig. 2B and fig. S4). The perimeter length increased linearly during its formation with the same velocity v_{growth} as it decreased upon lamellipod contraction (Fig. 2C), suggesting that similar processes drive these separate

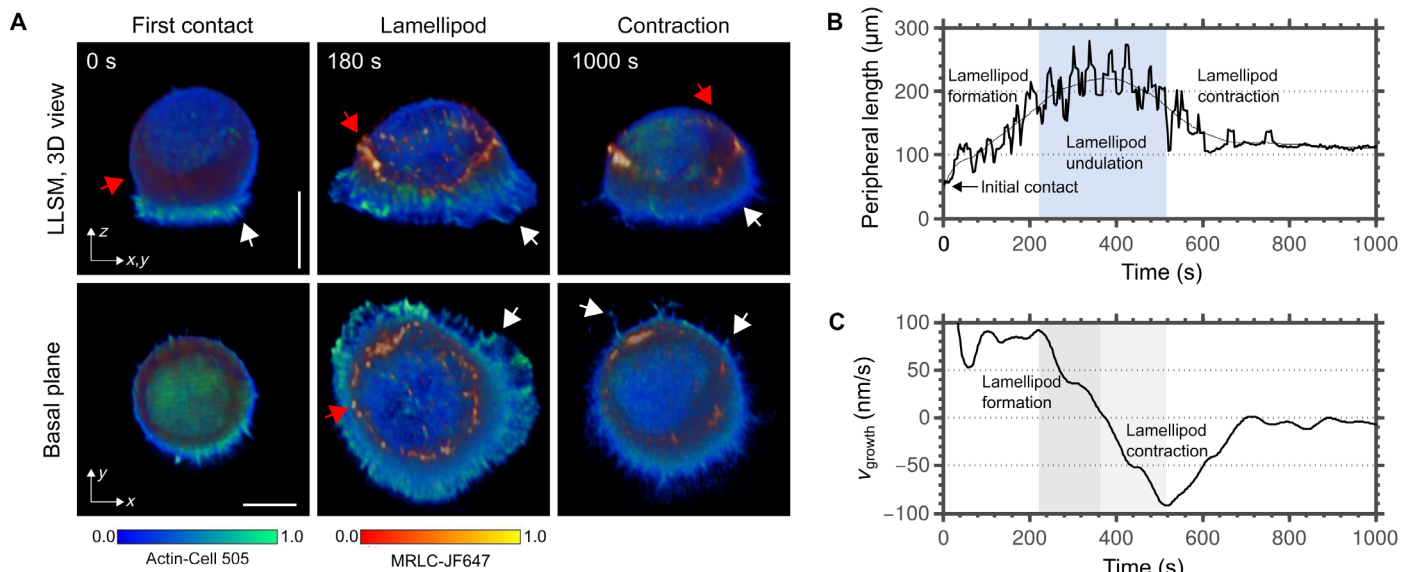


Fig. 2. Global actin cytoskeleton rearrangements during T cell activation: LLSM of 3D cytoskeletal reorganizations in Jurkat T cells over time when making contact with surfaces coated with activating antibodies. (A) Representative LLSM images of F-actin (blue to green, labeled with SNAP-tag and with the SNAP-tag dye-ligand Cell 505) and myosin-II motor proteins (red to orange, labeled with HaloTag and with the HaloTag dye-ligand JF647) at different time points after initial contact (as labeled); side view of whole cell (top) and bottom view of basal plane (bottom). Scale bar, 5 μm . T cells formed a ring-like symmetric contact with the surface (0 s, white arrow, left), followed by the formation and undulation (180 s, white arrow, middle) and retraction of a lamellipod (300 s, white arrow, right), accompanied by a distinct ring of myosin-II (red arrow), marking a boundary between peripheral lamellipodial and central actin structures. (B) Quantification of the changes in the peripheral length of the lamellipod's leading edge (as taken from fig. S4), illustrating lamellipod formation, undulation, and contraction. (C) Velocity v_{growth} of the change in peripheral length of derivative over time. v_{growth} varies as well yet with an identical growth and contraction speed.

events. After contraction (~10 min after contact), the contact area remained constant (40 of 40 investigated cells; Fig. 2, B and C). The changes in contact area size correlated with variations in cell height: decreasing during lamellipodium formation, fluctuating around a constant during lamellipodium undulation, and increasing during retraction (40 of 40 investigated cells; fig. S5).

Myosin localized toward the edge of the basal plane upon contact and remained behind the leading edge during lamellipodium formation and undulation (39 of 40 investigated cells) but moved inward during contraction (faint red ring in fig. S4). In addition to its dynamics at the basal plane, myosin-II was organized in a ring-like manner above the equatorial plane of the T cell during lamellipodium undulation and contracted with the cell body during the retraction phase (Fig. 2A). Myosin marks a clear boundary between peripheral lamellipodial and central F-actin structures, potentially stabilizing this separation, consistent with the findings of Ilani *et al.* (33).

Although LLSM allows us to investigate the overall cellular actin dynamics, this microscope under our measurement conditions did not have sufficient spatial resolution to observe in detail the underlying changes in cytoskeletal network structure that would lead to the formation of the symmetric boundary. For this, we turned back to super-resolution STED microscopy.

Nanoscope details of global actin rearrangements and symmetric boundary

We allowed the T cells to make contact with the glass surface and prepared different samples fixed at varying time points [1-min intervals, changing to cytoskeleton buffer at the time point of fixation to maintain the fibrous actin structures (22)], where fluorescent labeling of the cytoskeleton was achieved with Alexa Fluor 488-phalloidin and

its spatial organization at the basal membrane was imaged using STED microscopy (lateral resolution of ~60 nm; fig. S1). Consistent with the LLSM data, we identified the three stages of actin rearrangements at the following time points: 60, 180, and 900 s (Fig. 3). One minute after contact, the initial interface was symmetrical, with a torus-shaped central actin structure in the form of a ring and a peripherally forming lamellipodial actin network; both actin structures comprised a very dense network of filaments (32 of 32 investigated activating cells). The distinct lamellipod emerged at 3 min in the form of a larger ring-like actin network, mainly made up by densely organized short filaments that were still not fully resolvable. This dense F-actin structure was overlaid by a second actin network composed of very long filaments of average length $l_{\text{am}} = 5 \pm 1 \mu\text{m}$ (32 of 32 investigated activating cells), which pointed toward the center of the cellular interface. As discussed above, no actin network was observable in the basal plane in the center of the interface up to 3 min after initial contact (32 of 32 investigated activating cells). Finally, following contraction at 15 min, only a faint, contracted actin ring and actin “spikes” with an average length $l_{\text{spike}} = 3.0 \pm 0.7 \mu\text{m}$ (32 of 32 investigated activating cells) remained in the lamellipodium, with the spikes radiating toward the center. These experiments confirm that T cells form a symmetric interface at the time of initial contact and highlight the existence of a distinct symmetric boundary between peripheral lamellipodial and central structures. Over time, this symmetric structure laterally transforms into the described inward-growing ramified actin network and the centripetally outward-growing ring-like lamellipodial network.

Global actin cytoskeleton and TCR rearrangements

The characteristic architecture of the central ramified actin network raises the question on how this network might be involved in IS formation.

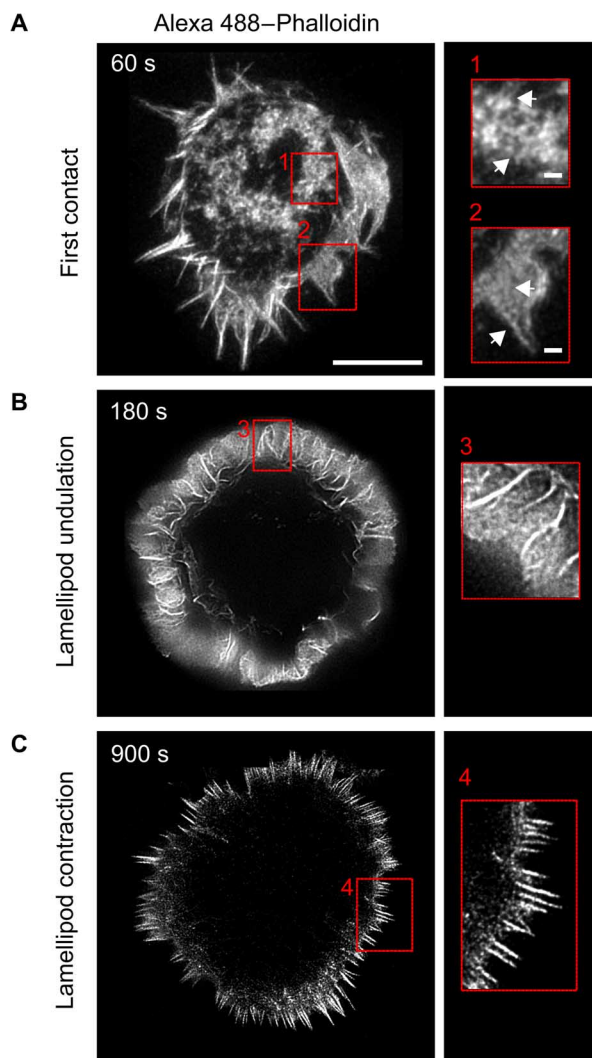


Fig. 3. Nanoscopic details of global actin cytoskeleton rearrangements during T cell activation. 2D STED microscopy of the actin cytoskeleton (labeled with Alexa Fluor 488-phalloidin) in Jurkat T cells fixed at different time points (**A**: 0 s, **B**: 180 s, **C**: 300 s) after making contact with surfaces coated with activating antibodies; overview images (left) and zoom-ins of red boxed areas (right); scale bars, 5 μ m (left) and 500 nm (right).

It has been shown that during T cell activation after contact formation with antigen-presenting surfaces, the actin cytoskeleton, and especially the lamellipodium, generates mechanical force in the direction of the interface center for translocating TCR microclusters, toward the center of the IS (13). For this reason, we were interested in how TCR molecules rearrange in our experiments for Jurkat T cells making contact with our activating surfaces. To address this question, we combined interference reflection microscopy (IRM) with fluorescence imaging of fluorescently tagged TCR (labeled with the organic dye JF647 via a SNAP-tag). The latter highlights any reorganization of the TCRs, whereas IRM allows monitoring the basal contact to the microscope cover glass (see Materials and Methods). We observed that the TCR is homogeneously distributed at the periphery of the interface during immediate contact formation. TCRs then accumulated homogeneously beneath the lamellipodium during undulation (fig. S6 and movie S4), followed by its slow translocation toward the center of the interface dur-

ing contraction (36 of 38 investigated cells; fig. S6 and movie S5); that is, it correlated with the overall actin reorganization dynamics, and the transport of the TCRs coincided with the formation of the central ramified actin network. The latter's similarity to a transportation network suggests that this structure could facilitate inward-directed motion of TCR microclusters.

Nanoscale changes in actin cytoskeletal network structure

Following the global rearrangements of cortical actin, we also sought to understand the nanoscale reorganizations of the actin cytoskeleton underpinning T cell activation. For this, we first focused on the diffusion dynamics of monomeric actin (G-actin). Formation of the ramified actin network and the observed changes in the actin mesh sizes may specifically affect G-actin diffusion and hence actin polymerization, which would, for example, explain the abrupt switch from actin ruffles to lamellipod formation. To this end, fluorescence correlation spectroscopy was used to compare the diffusion of fluorescently tagged G-actin (labeled via a SNAP-tag with the membrane-permeable SNAP-Cell 505-Star dye-ligand) at different cytosolic locations in the T cells at different stages. Under all conditions, whether in suspension or on activating antibody-coated glass or following depolymerization of the entire actin network with 1 μ M of the actin-sequestering drug latrunculin B, the G-actin monomers exhibited the same diffusion coefficient of $D \sim 15 \mu\text{m}^2/\text{s}$ and no obvious sign of anomalous diffusion (218 of 220 investigated activating cells; fig. S7), reflecting a low degree of molecular crowding. Therefore, limited G-actin diffusion does not explain the abrupt switch from actin ruffles to lamellipod formation.

Next, we determined the dynamics of F-actin. To quantify the growth kinetics of actin filaments as determined by turnover of actin protomers and to calculate the microscopic filament lengths, we combined computer simulations with fluorescence recovery after photobleaching (FRAP) experiments on labeled G-actin monomers in the cellular cortex (Supplementary Materials) (21, 23, 29). In the FRAP experiments, the recovery of fluorescence mainly reflects the monomers' binding kinetics to growing filaments (that is, their turnover kinetics, which determine F-actin growth rates and sizes) and, consequently, F-actin network stiffness, as further outlined below (21, 29). We detected small but significant changes in the turnover half-times between T cells in suspension (42 of 42 investigated suspended cells) and T cells making contact with the activating antibody-coated glass surface (46 of 46 investigated activating cells; Fig. 4, A to D, and table S1). More detailed analysis of the recovery curves identified two distinct turnover processes contributing to the global turnover half-time (Supplementary Materials and Fig. 5A), similar to previous studies of HeLa and M2 cells (21): a fast process dominant at short time scales accounting for 90% of the recovery and a slower process dominant at longer time scales (42 of 42 investigated suspended cells). To identify the filament subpopulations contributing to these distinct turnovers, we took advantage of their different responses to cytochalasin D (cytD), a potent inhibitor of actin polymerization. Using different concentrations of cytD (1 to 10 μ M) allowed us to distinguish between cytD-sensitive and typically short filaments that grow with faster turnover times and free barbed ends, that is, in a formin-independent manner (which have been shown to be Arp2/3-nucleated) (21, 22, 29), and the typically long cytD-insensitive formin-mediated filaments, which exhibit longer turnover times (42 of 42 investigated suspended cells). To rule out the existence of other cytD-insensitive filament populations, we confirmed

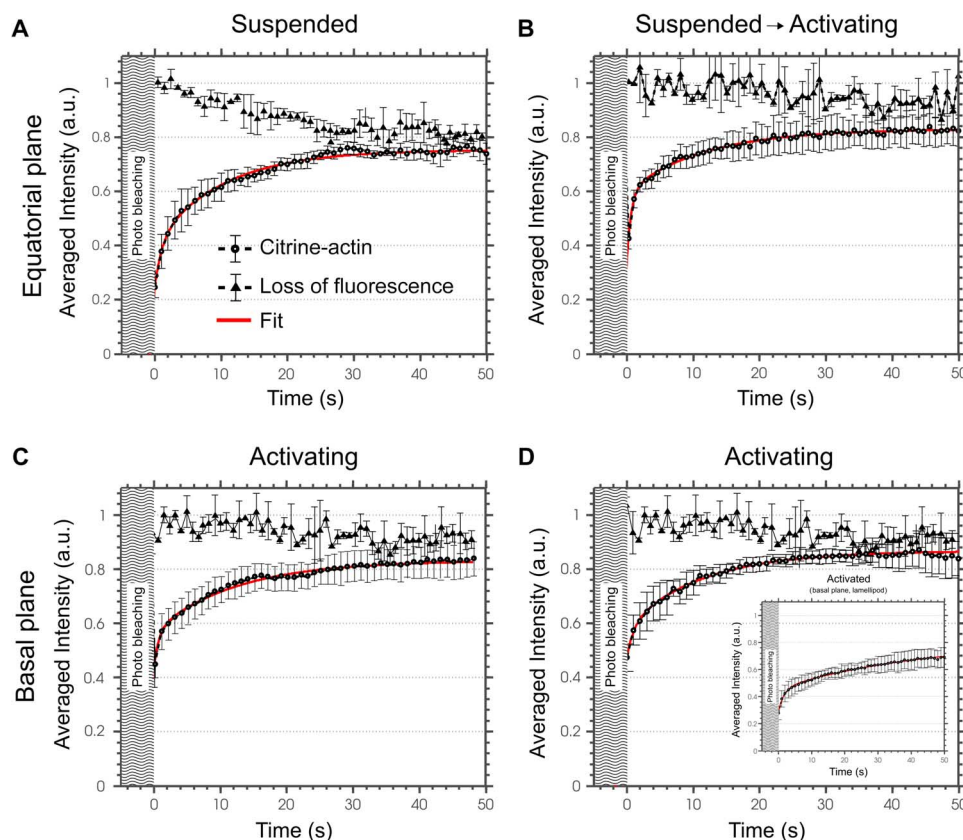


Fig. 4. Actin turnover dynamics measured in FRAP experiments for citrine-actin in Jurkat T cells under different conditions. Fluorescence recovery over time after photobleaching event at time 0: experimental data (citrine-actin, black dots), control from unbleached region (loss of fluorescence, black triangles) and biexponential fit to the data (red). Values were averaged, and error bars represent SDs from N measurements. **(A)** Equatorial plane of suspended Jurkat T cells with average recovery half-time $t_{1/2} = 6.3 \pm 0.6$ s ($n = 46$). **(B)** Equatorial plane of suspended Jurkat T cells under addition of soluble anti-CD3 ϵ and anti-CD28 antibodies, $t_{1/2} = 7.5 \pm 0.8$ s ($P < 0.01$ compared to suspended conditions, $n = 30$). **(C)** Equatorial plane of Jurkat T cells activated on anti-CD3 ϵ - and anti-CD28-coated glass, $t_{1/2} = 6.8 \pm 0.8$ s ($P < 0.01$ compared to suspended conditions, $n = 42$). **(D)** Basal plane of the activated Jurkat T cells of (C), $t_{1/2} = 7.5 \pm 0.8$ s ($P < 0.01$ compared to suspended conditions, $n = 32$). The inset shows the respective graph measured in the lamellipodium with an average recovery half-time $t_{1/2} = 33 \pm 3$ s ($P < 0.01$ compared to suspended conditions, $n = 29$).

the sensitivity of the formin-mediated filaments to the specific inhibitor SMIH2 (small molecule inhibitor of formin homology 2 domains) (25 of 25 investigated suspended cells, Fig. 5B and table S2). Our FRAP data thus suggest that the cell cortex of T cells is composed of two F-actin subpopulations: long formin-nucleated F-actin (with long actin turnover times) and short Arp2/3-nucleated F-actin with free barbed ends (and fast turnover times).

Consistent with the global turnover measurements, the turnover rate of the formin-mediated filaments was ~ 1.5 -fold lower in activated T cells at both the equatorial plane (within the cell cortex) and the basal plane (within the rosette-like network) compared to suspended T cells (42 of 42 investigated activating cells, $P < 0.01$; Fig. 5, D and F). The formin-independent filaments mostly exhibited the opposite behavior, indicating that their reorganization was more frequent and faster in activated T cells (46 of 46 investigated activating cells, $P < 0.01$; Fig. 5, C and E). In the lamellipodium, the turnover rates were generally two- to fivefold lower than in the cytosol (Fig. 5, E and F).

Computer simulations incorporating the FRAP data were used to estimate the average filament lengths and the fraction of total actin network composed of formin-dependent and formin-independent filaments (Materials and Methods and Fig. 5, C to F, and fig. S8) (23). In

suspended T cells, Arp2/3-nucleated filaments were, as expected, on average shorter (average length of 70 ± 15 nm) than formin-nucleated filaments (350 ± 60 nm) (42 of 42 investigated suspended cells). The cortex of suspended T cells is composed of approximately equal amounts of Arp2/3-nucleated and formin-nucleated filaments. Activated T cells had 70% Arp2/3-nucleated filaments with an average length of 50 ± 8 nm and 30% formin-nucleated filaments with an average length of 500 ± 80 nm (46 of 46 investigated activating cells); that is, upon activation, the fraction of short Arp2/3-nucleated filaments increases and their length decreases, whereas the portion of formin-nucleated filaments decreases and their length increases. The length of lamellipodial filaments of activated T cells was overall much larger with approximately evenly distributed populations of Arp2/3-nucleated (2000 ± 200 nm) and formin-nucleated (100 ± 20 nm) filaments (46 of 46 investigated activating cells). Conclusively, the nanoscale actin organization (including the meshwork size), F-actin turnover rates, and filament lengths and populations adjusted dynamically during activation, accompanying the global rearrangement of the actin network.

Early calcium signaling

Cytoskeletal rearrangements proceed for minutes, yet initiation of T cell activation through early TCR signaling lasts only a few seconds. For this

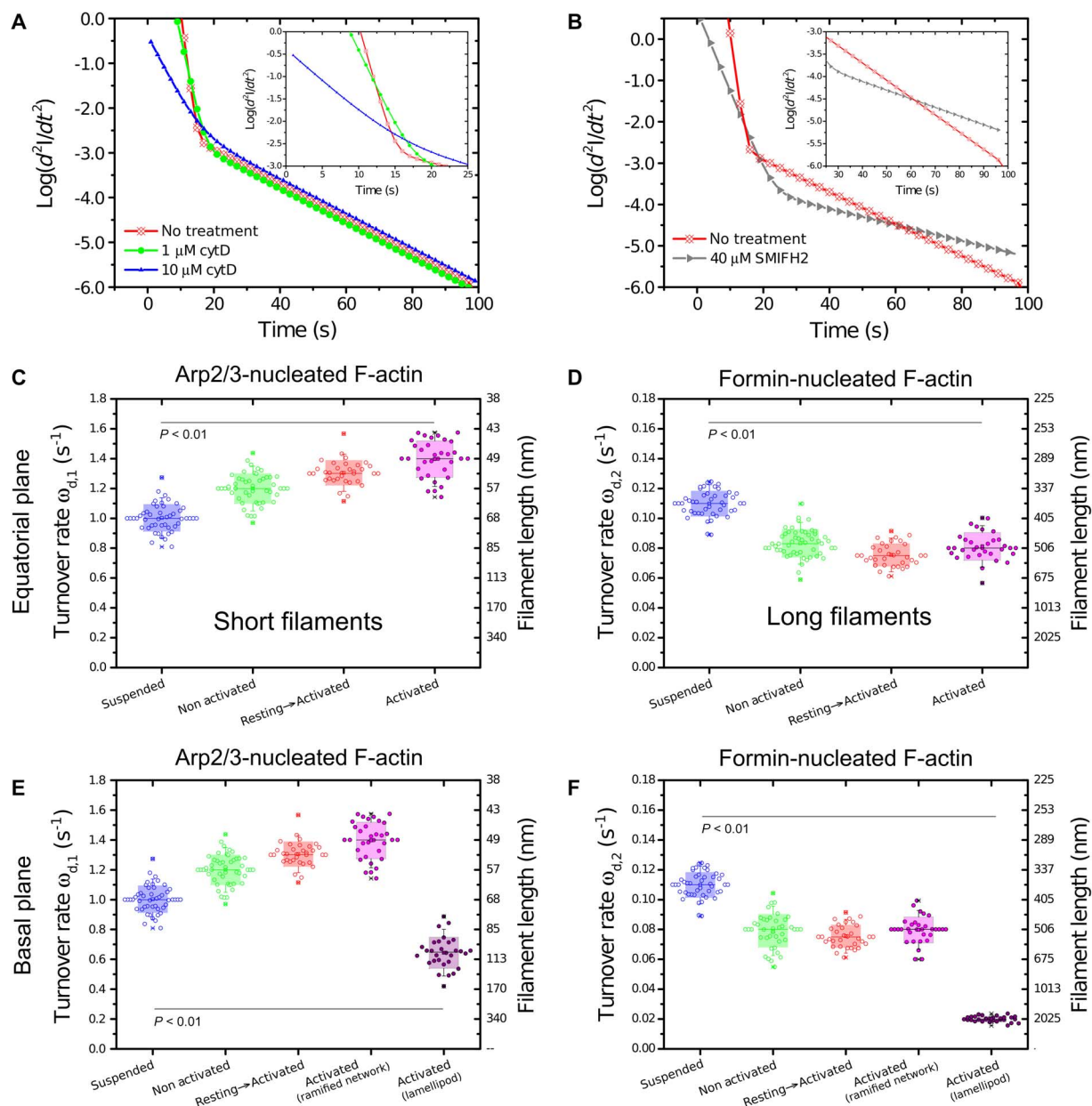


Fig. 5. Results from FRAP analysis of G-actin: actin turnover dynamics and filament lengths in the Jurkat T cell cortex and lamellipod. (A and B) Logarithmic acceleration plots [second derivative $d^2I(t)/dt^2$; see FRAP analysis] of the fluorescence recovery $I(t)$ in the FRAP experiments (A) after treatment with 1 μ M (green line, averaged over $n = 42$ cells) and 10 μ M (blue line, $n = 58$ cells) cytD and in the untreated case (red line, $n = 46$ cells) and (B) after treatment with 40 μ M SMIFH2 (red line, averaged over $n = 25$ cells) and in the untreated case (gray line). The insets present a close-up of the first 25 s (A) and 25 to 100 s (B). These experiments allowed the discrimination between cytD-sensitive, short Arp2/3-nucleated filaments (growing with the faster turnover times, that is, larger turnover rates), and long cytD-insensitive formin-mediated filaments (growing with longer turnover times, that is, smaller turnover rates) (compare table S2), although the sensitivity of the formin-mediated filaments to its specific inhibitor SMIFH2 ruled out the existence of other cytD-insensitive filament populations. (C to F) Boxplot of actin turnover rates $\omega_{d,1}$ and $\omega_{d,2}$ (left axes) and the corresponding filament lengths (right axes) for the different activating stages [Suspended, contact with nonactivating glass (Nonactivating), activation in suspension (Suspended \rightarrow Activating), and contact with activating glass (Activating)] and measured at the cell cortex in (C and D) the equatorial plane and (E and F) the basal plane for (C and E) the short formin-independent filaments and (D and F) the long formin-mediated filaments ($P < 0.01$ difference to suspended condition in all cases).

reason, the precise role of the actin cytoskeleton in early TCR signaling is poorly understood (39). This prompted us to next examine the relationship between the global rearrangement of the actin network and the early stages of T cell activation. For this, we relied on changes in calcium levels to monitor early TCR signaling. Using a time series of single-

plane spinning-disc microscopy images, we first quantified the increase in fluorescence of the calcium reporter Fluo-4 in individual T cells using the calcium quantification software CalQuo (45), upon very early contact formation with the activating antibody-coated glass surfaces. Color-coded maximum projections of the time stacks were used to

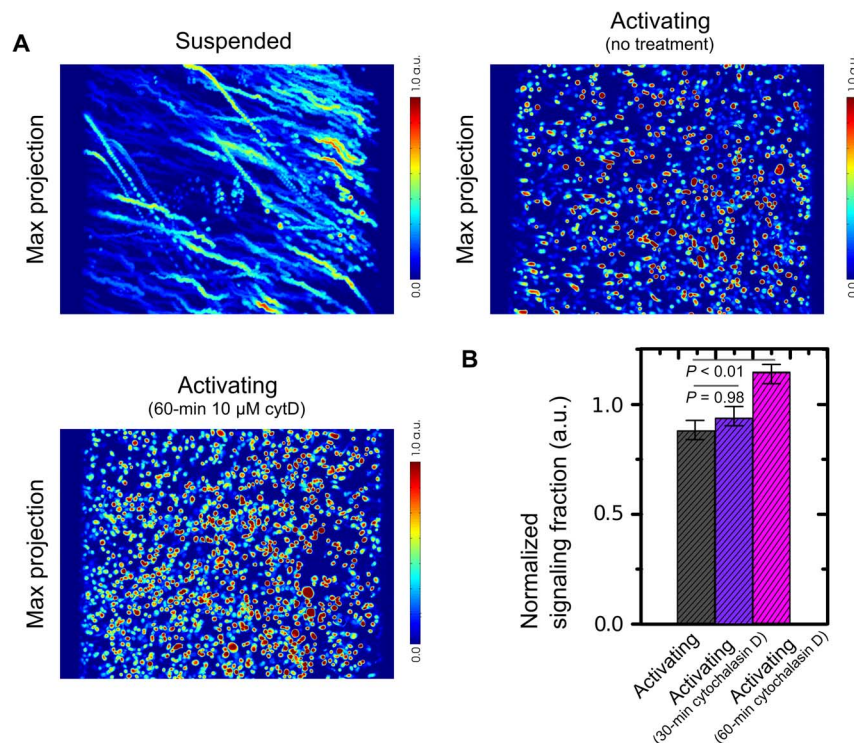


Fig. 6. Analysis of calcium response in the Jurkat T cells (signaling) using Fluo-4 for different conditions. (A) Maximum projections of fluorescence intensity over time for suspended cells (upper left) and cells making contact with anti-CD3 ϵ - and anti-CD28-coated glass without (right) and after treatment with cytD (lower left), as measured by a spinning disc confocal fluorescence microscope. Cold to warm colors represent low to high fluorescence intensities. Moving and signaling Jurkat T cells can be identified by a red dot with a blue tail. On average, <10% cells signaled under the suspended conditions, whereas about 80% signaled on activating glass. (B) Fraction of T cells revealing strong Fluo-4 emission and thus indicating strong calcium response (signaling fraction) when contacting the anti-CD3/CD28-coated (activated) and nonactivated glass surfaces with and without 30- and 60-min cytD treatment for inhibiting actin polymerization, as labeled. Fractions are normalized to the case of nontreated activating surfaces. Signaling fractions increased by 15 to 20% in both cases following treatment with cytD.

visualize signaling (Fig. 6A). As expected, we observed very high levels of calcium responses upon surface contact but not in T cells held in suspension (1500 to 2500 cells; Fig. 6B, fig. S9, and movies S6 to S8). For all cells producing calcium responses, the time period until triggering after first contact with the surface was ~ 60 s (fig. S9).

Early calcium signaling and global actin cytoskeleton rearrangements

To highlight the latter relationship between surface contact formation and early calcium signaling, we combined the calcium observation experiments with differential interference contrast (DIC) microscopy and IRM. The latter two techniques allowed us to monitor the apical surfaces of the T cells and their basal contacts, respectively (Fig. 7). Calcium signaling coincided with the immediate first contact of the T cell with the surface, after a 60-s period of ruffling without making contact, at a time point when less than an estimated $2 \pm 0.5\%$ of the cell was in contact with the surface and only actin ruffles were present. The macroscopic cytoskeletal rearrangements (such as cell polarization or formation of the lamellipodial and the ramified structures) consistently required an initial 25 s of contact following triggering (52 of 52 investigated cells; Fig. 7 and movie S9). This highlights the idea that although global actin reorganization accompanying IS formation only proceeds following contact formation to activating surfaces, early TCR signaling coincides with immediate first contact.

Global actin rearrangements in activating, suspended T cells

To further highlight the distinct impact of contact formation to activating surfaces, we investigated actin reorganization in T cells kept in suspension and then activated with soluble anti-CD3 and anti-CD28 antibodies. These T cells exhibited changes in turnover rates and filament lengths that are similar to those activated on anti-CD3 and anti-CD28 antibody-coated glass (30 of 30 investigated suspended cells; Figs. 4 and 5), suggesting that cortical ultrastructure reorganizes in response to T cell-activating signals per se, in a contact-independent manner. However, the T cells activated in suspension did not polarize but remained spherical, suggesting that surface contact is required to drive the profound macroscopic actin rearrangements observed on the activating glass surface. Nevertheless, calcium signals were generated when adding anti-CD3 and anti-CD28 antibodies to the suspended cells, indicating that full surface contact, such as lamellipodium formation, may not be necessary for early calcium signaling.

Early calcium signaling independent of global cytoskeleton rearrangements

Finally, we were prompted to further investigate whether full surface contact and lamellipodium formation are not required for early calcium signaling. We inhibited actin ruffle formation using 10 μ M cytD before initial contact with the activating antibody-coated surfaces. LSM imaging revealed that cytD impeded new ruffle formation, without affecting existing ruffles (15 of 15 investigated cells; fig. S10).

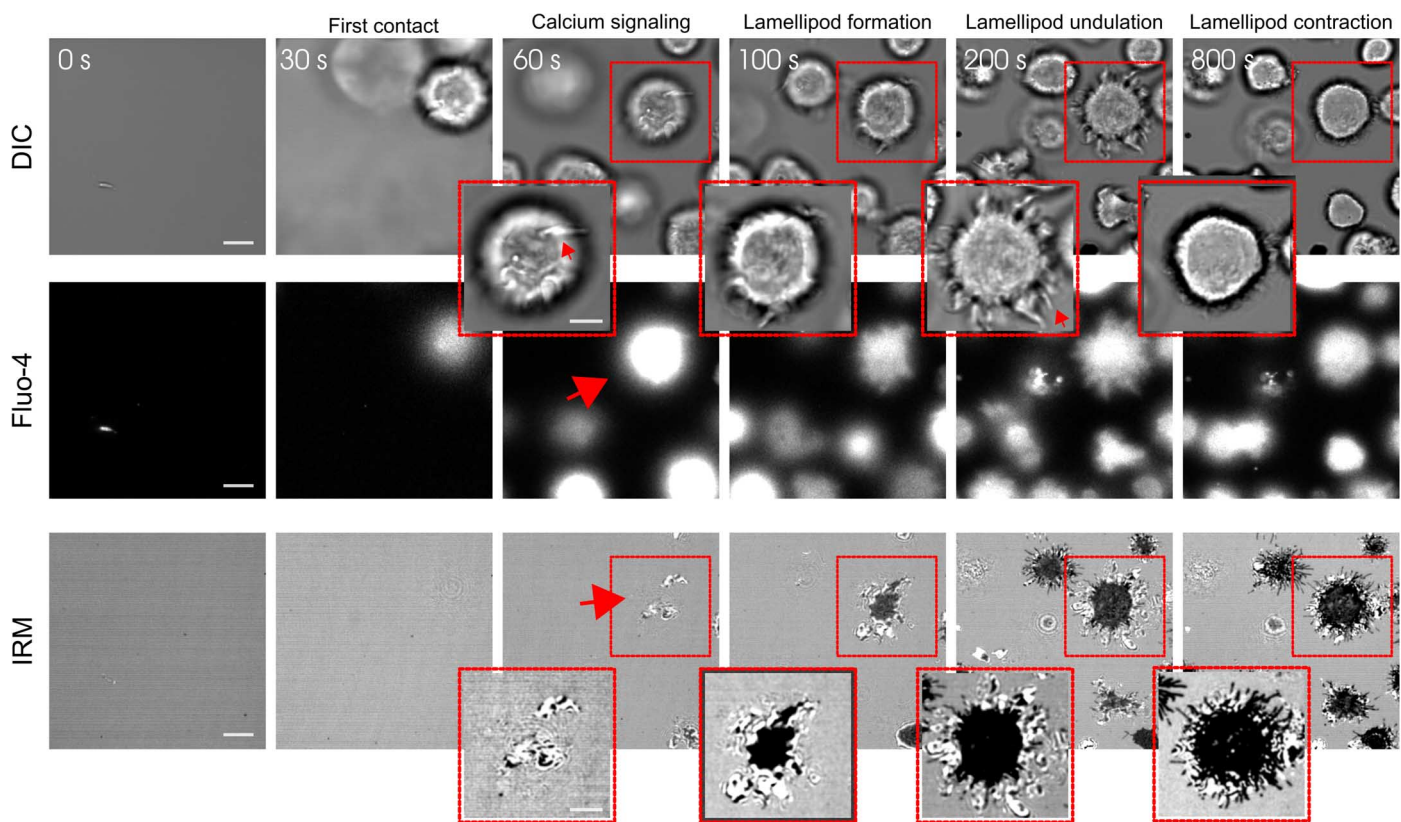


Fig. 7. Reorganizations of the T cell cytoskeleton following signaling. Representative concomitant time-lapse DIC (top), Fluo-4 fluorescence (middle), and IRM (bottom) images of live Jurkat T cells making contact with activating anti-CD3 ϵ - and anti-CD28-coated glass, revealing the cellular apical surface (cell polarization), calcium levels (T cell signaling), and basal contact area (lamellipod formation), respectively. Insets show DIC and IRM close-ups for the T cell marked in the respective images, whereas the red arrows in the DIC close-ups indicate ruffles (60 s) and lamellipodium (200 s); those in the Fluo-4 and IRM images reveal initial calcium response (DIC 60 s) and first contact (IRM 60 s). These experiments reveal that cytoskeletal reorganization occurred consistently after cell polarization and calcium response. Scale bar, 5 μ m.

We observed a marked reduction in cytoskeleton remodeling activity and subsequent actin rearrangements upon cytD treatment; T cells contacted the surfaces successfully, but the failure to produce new actin ruffles resulted in cell “wobbling” behavior, preventing the formation of a lamellipod and subsequent cytoskeletal reorganizations, including macroscopic TCR reorganization (fig. S10 and movie S10). However, preventing cytoskeletal reorganization did not inhibit early calcium signaling. On the contrary, 15% more T cells produced early calcium responses following treatment with cytD during contact with the activating antibody-coated surfaces (2112 of 2508 investigated cells; Fig. 6 and movie S11). Our observations thus highlight the fact that the initiation of IS formation, as revealed by calcium release, itself requires markedly little contact with activating surfaces and no cytoskeletal rearrangements.

DISCUSSION

Using a range of complementing advanced optical microscopy tools on both suspended and activating live and fixed Jurkat T cells, we have been able to demonstrate how a complex series of global cytoskeletal rearrangements across the whole cell accompany the formation of a ramified actin network, which underpins the formation of the IS. Although no actin network was observable immediately adjacent

to the basal plane in the center of the interface after T cell activation [using contact formation to activating surfaces, consistent with previous TIRF measurements (2, 9, 10, 13)], 3D reconstructions of the STED microscopy images of the actin cortex revealed the presence of a previously unreported distinct filamentous structure at the contact center. This coarse actin network, which formed 150 to 300 nm above the plane of surface contact, was connected to the lamellipodial network at the leading edge of the interface, producing a central ramified cytoskeletal structure. The structure of the ramified actin network is distinct from other actin networks, including cortices, lamellipodia, or lamella (22, 46). Its spatial characteristics disclosed a so-called inward-growing transportation network. Specifically, it comprised a unique orientation of its constituent actin filaments, pointing toward the center of the network.

Complementary measurements of TCR dynamics revealed correlations between this inward-growing transportation network and TCR dynamics. TCRs are first homogeneously distributed at the periphery of the contact, then accumulate, and finally slowly translocate toward the center of the interface. The latter transportation supports the correlation between TCR dynamics and actin reorganization and the involvement of the transportation network; that is, our observations suggest an involvement of the central ramified actin network in micro-cluster translocation (34), as also suggested by biphasic SLP-76 mobility

patterns (10). Our observed TCR dynamics are reminiscent of observations for T cells interacting with supported lipid bilayers (32, 47–49) but differ from the findings of Bunnell *et al.* (2). The authors did not observe TCR translocations presumably because of the absence of integrin binding and the higher-affinity activation antibody UCHT1. Unfortunately, we could not provide direct evidence for the ramified actin network to function as a transportation network. Simultaneous observation of TCR microcluster transportation and the propelling actin turnover dynamics of the ramified actin network remains technically challenging because they require dual-color super-resolution microscopy with extended spatial and substantial temporal resolution at a spatial location of 300 nm above the glass surface, which is beyond the technical possibilities of current super-resolution microscopy. The location of the network 150 to 300 nm above the microscope cover glass explains why this structure has not been seen in conventional TIRF studies, which penetrates only 50 to 100 nm into the sample.

We could confirm the global reorganization of the actin cytoskeleton and the presence and location of the ramified actin network in fixed PB cells. Unfortunately, systematic, state-of-the-art transductions of primary cells did not allow sufficient transfections of actin-associated proteins into primary cells because it would be required for the direct observation of actin dynamic in live PB cells using STED microscopy and LLSM.

LLSM observations revealed global cytoskeletal rearrangements both at the surface contact and over the whole cell body for periods of minutes to hours that led to the formation of the symmetric interface required for inward transportation networks and outward-growing lamellipodial structures. Following contact with the activating surface, the T cells polarized in the manner characteristic of migrating cells (50), by decreasing their height and extending and spreading evenly their leading edges. Following T cell spreading, undulations of a lamellipodium occurred at the contact, as seen previously (2, 10, 12, 13, 51), and the actin cytoskeleton was observed to contract during IS formation at later time points (to achieve full IS formation). Spreading occurred with the same velocity, comparable to Arp2/3-mediated F-actin turnover (23), as it decreased upon lamellipod contraction, suggesting that similar processes drive these separate events. Myosin-II may stabilize the symmetric boundary between peripheral lamellipod and central actin networks by creating two ring-like actin structures at the apical surface of the activating T cells and at the basal contact, the location of which was consistent with the observations of Yi *et al.* (52). The continuous undulations were reminiscent of the contractile lateral actin waves in lamellipodia reported in primary mouse T cells, supporting the notion of early cytoskeletal reorganizations in Jurkat T cells being similar to nontransformed and cytotoxic T lymphocytes (53).

Complementary STED microscopy images confirmed the sequence of changes in the lamellipodium (that is, spreading, undulation, and contraction) and, in addition, disclosed nanoscopic details of actin structure and rearrangement. Specifically, the STED microscopy images revealed that the symmetric contact observed in LLSM unfolded into a torus-shaped interface with the symmetric boundary required for strand formation and thus for growth inward into the ramified actin network and outward into the lamellipodium. Notably, previous super-resolution microscopy images of actin structures in other cell lines struggled to visualize these details of cortical networks owing to their dense cortical meshes [for example, 10 to 15 nm in cervical HeLa and melanoma cells (54)]. The actin meshwork was readily

resolved in Jurkat T cells owing to the much larger meshwork diameter of 150 to 200 nm in the cytosol and at the contact. In line with the mesh sizes observed using STED, the turnover rates and filament lengths of the cortical actin were fivefold larger in T cells than in non-lymphocytes (21, 23).

Comparisons of the actin meshworks of T cells held or activated in suspension and T cells forming contacts with nonactivating and activating surfaces revealed qualitatively very different morphologies and quantitatively different actin network structures compared to T cells interacting with plain and antibody-coated glass surfaces. Specifically, these comparisons revealed that the actin cytoskeleton reorganizations leading to IS formation were contact- and activating antibody-dependent. Although nanoscopic reorganization of the actin cytoskeleton (for example, changes in meshwork size, filament lengths, or actin turnover dynamics) also occurred when adding activating antibodies to the suspended T cells or after forming contacts with nonactivating surfaces, macroscopic actin cytoskeleton reorganizations, such as the formation of the lamellipod or ramified network, only occurred for activating surfaces. Nonspecific activating signals, such as IgG-activating conditions, did not translate into cytoskeletal reorganizations, implying that strong activation signals are needed for the drastic global changes seen as observed on OKT3 functionalized glass. The profound cytoskeletal reorganization we observed was therefore induced by engagement and triggering of the TCR.

Despite the changes in meshwork size, that is, increase in potential crowding during activation, G-actin exhibited no obvious sign of anomalous diffusion for any condition, suggesting limited molecular crowding and well-optimized actin utilization by the cytoskeletal networks and indicating that actin assembly and, ultimately, cortical F-actin lengths were not limited by actin monomer diffusion (23).

From FRAP measurements on fluorescently tagged G-actin, we characterized the nanoscale structure of the T cell cortex in unprecedented detail and found that it is composed of two F-actin subpopulations, long formin-nucleated F-actin and short Arp2/3-nucleated F-actin, consistent with the findings of Fritzsche *et al.* (23), with the ratio of populations and filament lengths changing upon activation. Whereas the size of formin-nucleated filaments increased, the respective opposite effect was observed for the Arp2/3-mediated filaments. The observation that formin seems to stabilize IS formation is consistent with a previous analysis (5, 33, 55). From a mechanical point of view, increasing the average length of larger formin-nucleated actin filaments likely produces a higher degree of cortical elasticity and therefore greater structural integrity and IS stability as well as a flatter and stiffer contact interface, a property that results in an efficient distribution of forces across the whole contact (23, 56). In contrast, the shorter and dynamic Arp2/3-nucleated filaments, despite their higher abundance, usually contribute little to cortical elasticity (23). However, they might contribute to a rapid reaction process, allowing cells to respond, for example, to TCR signaling by rapidly adjusting their turnover and length (17, 57). A relatively stiff cortex implies that T cell activation and/or IS formation depends on mechanical forces created by the actin cytoskeleton acting at the cell contact. Primary dendritic cells (DCs) form mechanosensitive podosomes at the contact periphery of the IS with T lymphocytes (9, 55). This supports the notion that T cells and DCs dynamically measure the stiffness of contact interfaces to adjust the underlying actin assembly dynamics, highlighting the

requirement of precisely measuring mechanical forces at cell contacts [see, for example, related studies (58–60)].

Calcium signaling in conjunction with IRM and phase-contrast imaging revealed that signaling coincided with the immediate first contact of the cell with the surface, well before lamellipodium formation. Even T cells activated in suspension generated some calcium signals, despite the fact that they did not polarize under these conditions and thus did not drive the profound macroscopic actin rearrangements leading to IS formation. In line with these observations, inhibition of cytoskeletal remodeling with cytD slightly enhanced rather than suppressed early calcium signaling, revealing that cytoskeleton-generated forces are not required for receptor triggering *per se*. However, independent of the cytD treatment, the time period until triggering after initial contact with the surface was the same, suggesting a specific biological response rather than a physical response due to mechanical interactions with the glass surface during initial contact.

Recently, CD45 was found to be segregated from kinase-containing regions of “close contacts” of T cells with surfaces coated with non-activating antibodies before TCR triggering occurs (61). CD45 segregation in this way is enough to initiate signaling, indicating a potential specific biological response after initial contact. Our new observations suggest that the early binding of integrins of the cell combined with cellular rigidity may be sufficient to passively induce CD45 segregation, leading to signaling in the presence of cytD.

Finally, our experiments show that the resting-cell cytoskeleton, characterized here by studying cells held in suspension, is devoted largely to “ruffle” formation and that calcium signaling requires the formation of markedly small contacts with an activating surface, underscoring the sensitivity of the TCR. Given the observations (i) that CD45 segregation over large areas of contact is sufficient to initiate signaling in the absence of ligands (61) and (ii) that preventing ruffle formation with cytD induced somewhat more rather than less signaling, it seems possible that the very dynamic process of cytoskeleton-driven ruffle formation prevents contacts from becoming too large, preventing or limiting nonspecific T cell signaling in this way. Computational simulations (62) have suggested a requirement for the formation of submicron-scale close contacts. Therefore, in addition to facilitating initial contact formation and, later, the generation of the IS through active rearrangements of membrane proteins, the cortical actin cytoskeleton may also serve to enhance the specificity of TCR-initiated T cell signaling.

In summary, we have disclosed a novel central ramified actin network in activated T cells from the bottom-up that is involved in IS formation and accompanied by a range of microscopic actin reorganizations and global rearrangements, for example, supporting a very flat and stiff contact at the IS interface. Unexpectedly, these processes are initiated during the earliest steps in T cell signaling, with markedly little contact required. We anticipate that our study provides a useful methodological blueprint for future studies focusing on the interplay between receptors, the signaling machinery, and components of the actin cytoskeleton in adaptive and innate immunity.

MATERIALS AND METHODS

Cell culture

Jurkat T cells were cultured in sterile RPMI (Sigma-Aldrich) supplemented with 10% FCS (PAA), 2 mM L-glutamine (Sigma-Aldrich), 1 mM sodium pyruvate (Sigma-Aldrich), 10 mM Hepes (Sigma-

Aldrich), and 1% penicillin-streptomycin-neomycin solution (Sigma-Aldrich). Cells were maintained at 37°C and 5% CO₂ during culturing, and handling was performed in HEPA-filtered microbiological safety cabinets. Typically, cells were kept at a density between 5×10^5 and 9×10^5 cells/ml.

Plasmids

The vector encoding human β -actin N-terminally tagged with mCitrine was generated by amplification of the ACTB gene by polymerase chain reaction (PCR) using oligonucleotide primers with cDNA from human embryonic kidney (HEK) 293T cells as template. The product contained ACTB flanked by 5' Bam HI and 3' Not I restriction nuclease sites and followed by a TAG STOP codon. Following digestion with Bam HI and Not I, this was ligated into a pHR-SIN lentiviral expression vector containing the mCitrine gene upstream of the Bam HI site in the correct reading frame. Sequence integrity was confirmed by reversible terminator base sequencing.

To obtain vectors C-terminally tagged with LifeAct-citrine, LCK-SNAP, and TCR-SNAP (New England Biolabs), we amplified the genes by PCR to produce double-stranded DNA fragments encoding LifeAct, LCK, and TCR sequences followed by a Gly-Ser linker and flanked by 5' Mlu I and 3' Bam HI restriction nuclease sites. Following digestion with Mlu I and Bam HI, this was ligated into pHR-SIN lentiviral expression vectors containing the mCitrine gene downstream of the Bam HI site in the correct reading frame. Sequence integrity was confirmed by reversible terminator base sequencing.

Generation of stable cell lines

Jurkat-derived T cell lines stably expressing LifeAct-citrine, mCitrine-actin, LCK-SNAP, and TCR-SNAP were generated using a lentiviral transduction strategy. HEK-293T cells were plated in six-well plates at 3×10^5 cells/ml, 2 ml per well in Dulbecco's modified Eagle's medium (Sigma-Aldrich) + 10% FCS (PAA). Cells were incubated for 24 hours at 37°C and 5% CO₂ before transfection with 0.5 μ g per well each of the lentiviral packaging vectors p8.91 and pMD.G and the relevant pHR-SIN lentiviral expression vector using GeneJuice (Merck Millipore) as per the manufacturer's instructions. Forty-eight hours after transfection, the cell supernatant was harvested and filtered using a 0.45- μ m Millex-GP syringe filter unit to remove detached HEK-293T cells. Three milliliters of this virus-containing medium was added to 1.5×10^6 Jurkat T cells in 3 ml of supplemented RPMI medium. After 48 hours, cells were moved into 10 ml of supplemented RPMI and passaged as normal.

Isolation of human PB CD4⁺ T cells

Peripheral blood mononuclear cells (PBMCs) from the blood of three healthy adult volunteers were isolated by density gradient centrifugation. CD4⁺ T cells were isolated from PBMCs using the CD4-negative selection kit from Miltenyi Biotec UK, following the manufacturer's recommendations. The purity of CD4⁺ T cells ranged from 97 to 99% from total lymphocytes.

Microscope coverslip preparation

Microscope coverslips were functionalized for testing Jurkat T cell activation by coating with IgG plus anti-CD3 ϵ and anti-CD28 antibodies or IgG only. Coverslips with a diameter of 25 mm (SLS) were coated with 1 ml of donkey anti-mouse IgG antibody (50 μ g/ml) in coating buffer [50 mM Na₂CO₃ and 50 mM NaHCO₃ (pH 9.6), filtered using a 0.22- μ m Millex-GP syringe filter unit] overnight at 4°C in six-well plates. Coverslips were washed three times with 1 ml of

phosphate-buffered saline (PBS) and blocked for 3 hours at room temperature using RPMI + 10% FCS. For anti-CD3 ϵ and anti-CD28 antibody coating, the coverslips were again washed three times with 1 ml of PBS and coated with 1 ml of mouse α CD3 ϵ (Jackson ImmunoResearch, clone: OKT3) and mouse anti-CD28 (eBioscience, clone: CD28.2) at 5 μ g/ml each in PBS overnight at 4°C. Coverslips were washed a final time with 3 \times 1 ml of PBS before use.

Cell fixation

Jurkat and PB CD4⁺ T cells were washed and resuspended in cytoskeleton buffer [50 mM imidazole, 50 mM KCl, 0.5 mM MgCl₂, 0.1 mM EDTA, and 1 mM EGTA (pH 6.8)] at a concentration of 2.5×10^6 cells/ml. Coverslips were submerged in 1 ml of cytoskeleton buffer in six-well plates, and 100 μ l of cells was added dropwise evenly across the surface of the coverslip. Cells were incubated for varying amounts of time at room temperature, after which the cytoskeleton buffer was replaced with 1 ml of cytoskeleton buffer containing 0.25% glutaraldehyde and 0.5% Triton X-100, with care taken not to disturb the cells attached to the glass. Samples were fixed for 5 min at room temperature before they were washed in 2 \times 1 ml of cytoskeleton buffer and covered with 1 ml of cytoskeleton buffer containing 33 nM Alexa Fluor 488–phalloidin (Life Technologies) for 30 min and then finally washed three times with 1 ml of cytoskeleton buffer before imaging.

SNAP-tag and HaloTag labeling

Cells expressing the SNAP-tag (New England Biolabs) and/or HaloTag (Promega) fusion protein were labeled following the manufacturer's preparation protocol (www.neb.com and www.promega.co.uk). The cell medium was first replaced with 200 μ l of SNAP-tag (or HaloTag) medium [Leibovitz's L-15 medium (Life Technologies) with 1 to 5 μ M SNAP-tag (or HaloTag) ligand] and then incubated for 45 min at 37°C at 300 rpm. Finally, to ensure that free dye would not remain in the cytoplasm, the cell-labeling solution was washed three times in L-15 and then further incubated for 30 min at 37°C at 300 rpm.

Suspended T cells

CyGEL Sustain (Abcam) was used to suspend Jurkat T cells in hydrogels with three layers of different gel concentrations. The first layer comprised 100% hydrogel, the second layer comprised 50% hydrogel, and the third layer comprised 25% hydrogel, following the manufacturer's preparation protocol. Hydrogel concentrations were diluted in Leibovitz's L-15 medium (Life Technologies). Cells were imaged at 37°C and 5% CO₂.

Activation of suspended T cells

Suspended Jurkat T cells were activated by pipetting soluble mouse α CD3 ϵ (OKT3) and mouse anti-CD28 (eBioscience, clone: CD28.2) at 10 μ g/ml each in PBS directly into the microscope sample. Cells were imaged at 37°C and 5% CO₂.

Drug treatment

CytD, latrunculin B, and SMIFH2 were purchased from Merck Biosciences. Drugs were added to the culture medium at the given concentrations, and the cells were left to incubate for at least 10 min. Inhibitors were also present at the same concentration in the imaging medium.

Lattice light-sheet microscopy

LLSM was performed at the Advanced Imaging Centre, Howard Hughes Medical Institute, Janelia Research Campus, VA, using a 2D array of nondiffracting Bessel beams illuminating the specimen at a single plane.

The microscopy setup is described in the study of Chen *et al.* (44). Specimens were mounted on a 5-mm glass coverslip (#1 thickness, Warner Instruments) and secured in a custom-made surgical steel holder onto a piezo stage (Physik Instrumente). Fluorescently tagged Jurkat T cells were dispensed above the coverslip into the medium bath. All experiments were performed at 37°C and 5% CO₂. Once a cell of interest was within the focal plane of the light sheet, the sample was laterally scanned through the light sheet. The total scan distance ranged from 0 to 15 μ m at 10- to 40-ms exposure. Emitted photons were collected from the single excitation plane by a 1.1 numerical aperture (NA) 25 \times water-dipping objective (Nikon) and recorded on an Orca Flash4.0 V2 sCMOS camera (Hamamatsu). Cells were excited by either 488- or 560-nm wavelength laser light at 1 to 5% acousto-optic tunable filter transmittance of 300- and 500-mW laser power (MPB Communications).

Following data acquisition, all images were deskewed to correct for the 31.8° angle of the detection objective relative to the vertical axis of the sample and run through multiple iterations of a Richardson-Lucy deconvolution algorithm. Volumetric rendering and 4D visualization were carried out using Amira 3D Software for Life Sciences (FEI).

To characterize changes in cell height and the peripheral length of the cells' lamellipodium from LLSM 3D reconstructions (as shown in Figs. 2, B and C, and 5, A and B), a multistage image-processing protocol was performed. Before processing, each frame of the 3D image stack was normalized to its maximum intensity. Custom-written MATLAB routines were used to segment each frame of the 3D image stack by applying a threshold at an arbitrary low value (0.002), resulting in a binary image of the cell. This way, the cell was segmented throughout the whole plane and the cells' height or leading edge of the lamellipodium could be tracked for all frames.

Temporal projections were established by plotting the tracked edges onto one plane and by color-coding each frame with cold to warm colors representing early to late time points as shown in fig. S4. Peripheral lengths were then determined by calculating the total length of the tracked leading edges. To graphically visualize changes in the peripheral length, we plotted peripheral length against time, as presented in Fig. 2, A and B. Furthermore, to determine the velocity of these changes, we calculated the derivative in time using the MATLAB preimplemented function "diff," as presented in Fig. 2, A and B.

To characterize changes in cell height, a rectangular box was fitted to the 3D reconstruction of the cell for each frame of the 3D image stack. The total height of the box was then calculated for each frame. To graphically visualize changes in the cell height, we then plotted cell height against time, as presented in fig. S5A. Furthermore, to determine the velocity of these changes, we calculated the derivative in time using the MATLAB preimplemented function diff, as presented in fig. S5B. For each experimental condition, we acquired LSSM images from at least 15 individual cells over the course of at least three independent experiments.

STED microscopy

STED microscopy experiments were performed on a Leica TCS SP8 3 \times microscope (Leica). All live-cell experiments were performed at 37°C and 5% CO₂. The microscope was equipped with a pulsed supercontinuum white-light laser (WLL; 80 MHz, Koheras SuperK) for excitation and a 592-nm 1.5-W continuous-wave STED laser. Citrine and Alexa Fluor 488–phalloidin were excited at 488 nm, and fluorescence emission was collected at around 530 and 520 nm, respectively. For STED imaging, excitation laser intensities of 1 to 5%

of the WLL and 30 to 100% of the 592-nm STED laser were used to obtain a strong enough fluorescence signal as well as sufficient improvement in spatial resolution, and images were acquired at 1- to 5-s intervals to minimize loss of fluorescence due to photobleaching as well as cell phototoxic effects (of which we did not observe any in the recordings). All images were acquired on the Leica HyD detectors using time-gated detection with a time gate of 10 to 15 ns. The STED laser beam was split into two paths, each including a phase plate for creating the donut-like intensity focal patterns along lateral (xy) and axial (z) directions. By setting the relative allocation of the STED laser power between these two phase plates by use of a variable beam splitter, it was possible to tune the spatial resolution of the microscope along the xy and z direction individually.

Using the Huygens STED Deconvolution Wizard (Huygens Software), only a moderate degree of deconvolution was applied to the recorded STED images to avoid deconvolution artifacts. The microscope's point spread function (PSF) was directly calculated from the Leica imaging files, following standardized Huygens software guidelines (www.leica-microsystems.com/science-lab/huygens-sted-deconvolution-quick-guide/). For the maximum projections of the 3D STED image stacks, all images of a stack were projected onto one plane using custom-written MATLAB routines (MATLAB Inc.) and color-coded with respect to time or maximum fluorescence intensity.

The effective size of the STED microscope's PSF was determined using fluorescent microspheres [FluoSpheres, yellow-green (505/515), 0.04 μm diameter; Invitrogen] (fig. S1). This sample was prepared by diluting the beads in Milli-Q water with a dilution factor of 1:10,000. A drop of diluted beads was attached to the coverslide using poly-L-lysine (Sigma-Aldrich), and the coverslip was then mounted on a microscope slide and embedded in the mounting medium Mowiol. For each experimental condition, we acquired STED images from at least 40 individual cells over the course of at least three independent experiments.

F-actin orientation analysis

The simulated fiber geometries of inward- and outward-growing F-actin networks were computed in custom-written MATLAB (MATLAB Inc.) routines adjusted from (26). The orientation and isotropy properties of the actin filaments in a given region of an (experimental or simulated) image were computed based on the evaluation of the structure tensor in a local neighborhood using the Java plugin for ImageJ (<http://imagej.nih.gov/>) "OrientationJ." OrientationJ has four functionalities: visual representation of the orientation, quantitative orientation measurement, and marking distribution (<http://bigwww.epfl.ch/demo/orientation/>). Specifically, the user specifies the size of a Gaussian-shaped window, and the program computes the structure tensor for each pixel in the image by sliding the Gaussian analysis window over the entire image. The local orientation properties are computed and are then visualized as gray-level or color images with the orientation being typically encoded in color. The data presentation was performed in custom-written MATLAB routines (MATLAB Inc.). For each experimental condition, we analyzed the F-actin orientations from at least 45 individual cells over the course of at least three independent experiments.

F-actin mesh size

To characterize the actin mesh from the 3D STED images, as shown in fig. S3, a multistage image-processing protocol was performed. Before processing, each frame of the 3D image stack was

normalized to its maximum intensity. Next, for the part of the images containing the cell, the three bottommost frames were processed using a second-order steerable filter with $\sigma = 2.0$ (ImageJ, <http://imagej.nih.gov/>). The core actin mesh structure was then further refined to the most distinct structures through a "minimum" z -projection reducing the three image stacks to a single plane with the smallest intensity value across the z axis being retained at each pixel location (x,y). This processing resulted in a grayscale image that highlighted the actin mesh structure and was highly tolerant to variations in intensity across the image plane. We then applied a threshold at an arbitrary low value (0.002), resulting in a binary image of the actin meshwork (fig. S3). To establish the total area of the cell and of the mesh, we "filled" the binary image so that any gaps in the network were removed, and the cell was segmented throughout the whole plane. The number of pixels in the "unfilled" image and the filled image was then compared to give a percentage value of mesh density. To establish the size of the gaps in the mesh, the unfilled image was inverted, and the gaps within the mesh were characterized using the MATLAB "region props" function including the "EquivDiameter" and "Area" parameters. These parameters generated a circular area of equivalent size to the gap region and then determined the meshwork size of that specific gap as the diameter of the circle. The STED images have been recorded with a pixel size of 25 or 33 nm, resulting in the same values of actin mesh size. For each experimental condition, we analyzed the F-actin mesh sizes from at least 15 individual cells over the course of at least three independent experiments.

FCS analysis

FCS experiments were performed on the same Leica TCS SP8 3 \times microscope as described above. Cell 505-Star was excited using the WLL at 488 nm, and fluorescence was collected at around 530 nm using an external single-photon-counting avalanche photodiode (APD). The APD signal was registered by time-correlated single-photon-counting electronics (PicoHarp300, PicoQuant), which, in combination with its software (SymPhoTime), allowed for a fast calculation of the FCS correlation data out of the recorded signal. The experiments were performed at 37°C and 5% CO_2 and at a low excitation power (2 μW , 10% output of 30% master output). The duration of each measurement was 4 s, which followed a 1-s prebleaching of the focal spot to only include signal from diffusing actin monomers. Three repetitions were performed per position, and three different positions were chosen per cell.

The FCS data were analyzed using the SymPhoTime software (PicoQuant). The correlation data $G(\tau)$ (with correlation time τ) were fitted with a model of 3D diffusion, including an anomaly factor α

$$G(\tau) = G(0) \left[\left[\left(1 + \left(\frac{\tau}{\tau_D} \right)^\alpha \right) \cdot \left(1 + \left(\frac{\tau}{\tau_D \kappa^2} \right)^\alpha \right)^{0.5} \right]^{-1} \right]$$

Here, $G(0)$ is the correlation curve's amplitude, τ_D is the average transit time of the diffusing and labeled molecules through the observation spot, κ is the ratio of the axial and lateral diameters of the observation spot, and α is the anomaly factor (which is $\alpha = 1$ for normal free diffusion and $\alpha < 1$ for hindered diffusion, for example, due to spatial confinements due to molecular interactions with

slow-moving entities or molecular crowding). κ was fixed to 5 throughout the analysis. The data were fitted in the range $\tau = 10^{-2}$ to 10^2 ms. Data with $\alpha < 0.6$ were excluded from further analysis because these represented outliers (<1%) with a biased fit due to a very large noise level. For each experimental condition, we analyzed the diffusion dynamics from at least 200 individual cells over the course of at least three independent experiments.

FRAP experiments

FRAP experiments were effected as described by Fritzsche *et al.* (21, 29). FRAP experiments were performed at 37°C and 5% CO₂ using a 1.4 NA 100× oil immersion objective on a spinning disc fluorescence microscope (Zeiss Cell Observer Spinning Disc Confocal, Carl Zeiss AG). The fluorescent protein citrine was excited at 488 nm, and fluorescence emission registered at around 525 nm. In the FRAP experiments, a small circular region of interest (radius $r = 2 \mu\text{m}$) centered on the cell membrane was imaged, and a smaller circular bleaching region ($r = 1 \mu\text{m}$) was chosen in its center. This choice of imaging and bleaching modes minimized the fluorescence loss due to photobleaching during the recovery as well as phototoxic effects on the cell by not exposing the whole cell to light but restricting illumination and thus photobleaching to a section of only 0.6 μm in thickness (29). Bleaching was performed by scanning the 488-nm beam operating at 100% power of the 20-mW laser. In our protocol, bleaching was realized with a single laser pulse of 2 s during which scanning was performed with a pixel dwell time of 8 μs . The recovery of fluorescence was monitored at the same scanning speed with 1 to 5% of the laser power over 100 frames at 0.05- to 1-s intervals to minimize photobleaching but still allow sampling at a sufficient enough speed (29). For each recovery, two time-lapse image streams were recorded before the initial bleaching, which realized normalization of the fluorescence signal. To assess the loss in fluorescence during observation of the recovery (due to photobleaching), we selected the simultaneously recorded fluorescence signal from a nonbleached region. In all cases, the rate of fluorescence loss due to the observation of recovery was significantly smaller than the rates of fluorescence recovery, with a characteristic time of ~ 500 s, which was one order of magnitude larger than the slowest recovery time scale observed for actin. Hence, imaging-induced fluorescence loss did not significantly affect turnover measurements. For each experimental condition, we acquired FRAP recovery curves from at least 30 individual cells over the course of at least three independent experiments.

FRAP analysis

FRAP data analysis was effected as described by Fritzsche *et al.* (21, 29). The total fluorescence signal at the cortex interface resulted from proteins bound to the actin cortex and proteins freely diffusing in the cortical actin. Therefore, recovery had contributions from (i) cytosolic diffusion (cytosolic diffusive recovery) and (ii) association/dissociation of proteins to the cortex (reactive recovery). Given the fast cytoplasmic diffusion ($D \sim 15 \mu\text{m}^2/\text{s}$ of actin in our experimental geometry), diffusion of monomers took place with a characteristic time scale of $\tau \sim r^2/4D \sim 50$ ms (with $r = 1 \mu\text{m}$ being the radius of the bleached zones), which was several-fold shorter than the characteristic times of the reactions examined in this study ($\tau \geq 500$ ms). Thus, given the acquisition rate used in this study (0.1 to 1 s per frame), diffusive recovery was complete by the time we acquired the first postbleach frame. Therefore, the fluorescence recovery we measured in our experiments was solely reactive. To determine how many first-order molecular processes contributed to turnover, we fitted cortical recovery $I(t)$ with a combina-

tion of exponential functions I_i of the form $I_i(t) \sim [1 - \exp(-t/\tau_{d,i})]f_i F_0$, where F_0 is the initial fluorescence of the bleached region and i is the molecular process participating to recovery. Each function I_i represents the contribution of the molecular process i to the total recovery, with f_i being the portion of the total protein population undergoing turnover process i ($\sum_i f_i = 1$) and $\tau_{d,i}$ being the characteristic dissociation time of process i . The characteristic dissociation time τ_d is inverse to the turnover rate $\omega_{d,i}$ and linked to the half-time reported in most FRAP experiments: $t_{1/2} = \ln(2) \tau_d$. If several molecular processes occur at similar time scales, they cannot be distinguished, and the apparent rate constant measured reflects an average over all of the molecular processes acting at that time scale. In practice, fluorescence recovery curves $I(t)$ were fitted with an increasing number of exponential functions until the following three conditions were met: the goodness of fit estimated through r^2 no longer increased, the total change in fluorescence associated with process n was less than 0.001%, and the sum of squared errors no longer decreased.

Hence, this approach allowed determination of the number of molecular processes i that contribute to fluorescence recovery, their characteristic turnover times $\tau_{d,i}$, and the portion f_i of the total protein population that recovered through process i . In this analysis, changes in the recovery half-time $t_{1/2}$ may have therefore resulted from changes in the number of processes i participating to recovery, changes in the characteristic times $\tau_{d,i}$ of some or all of the processes, changes in the relative importance f_i of some or all of the turnover processes, or a combination of all of these factors. Therefore, analysis of fluorescence recovery using multiexponential fitting allowed for a more precise characterization of turnover and the changes occurring in response to perturbations.

Logarithmic acceleration plots that represent the logarithm of the second derivative of the fit function (Fig. 5, A and B) were used to compare the turnover rate constants across experimental conditions and to visualize the different processes participating in the fluorescence recovery of the FRAP data. In these plots, each piecewise linear segment corresponds to a different fluorescence recovery process. The slope of each segment is characteristic for the turnover rate ω_d . Changes in the recovery rates in response to drug treatment or genetic perturbations will result in linear segments with steeper or shallower gradients. Further details can be found in the study of Fritzsche *et al.* (29).

FRAP computer simulation

Computer simulations were effected as described by Fritzsche *et al.* (23) and here used to calculate the actin filament length distributions, including average filament lengths out of the FRAP data for various conditions, as presented in figs. S6 and S7. Previously calibrated computer simulations (23) were used to reproduce the FRAP experiments by mimicking actin turnover dynamics. In the FRAP experiments, we found two types of F-actin with different turnover rates ($\omega_{d,1}$ and $\omega_{d,2}$): Long filaments were generated by formins and short filaments were nucleated by the Arp2/3 complex. Practically, all simulation parameters (see below) were varied until all four FRAP fitting parameters fully matched $\omega_{d,1}$, $\omega_{d,2}$ and f_1, f_2 , whereas the goodness of the fit estimated through r^2 no longer increased, the total change in each parameter was less than 5%, and the sum of squared errors no longer decreased. In this way, the simulation output delivered the distribution of the actin filament lengths.

Stochastic simulations of the cortex were carried out by following a Gillespie scheme. The state of the cortex was determined by its number of filaments, their lengths, and the states of the monomers constituting

the filaments. Filaments were represented by linear arrays of varying lengths. The entries in the array specified the state of the corresponding monomer, where we distinguished between fluorescing and nonfluorescing monomers. In addition, filament plus-ends could be bound to formin, whereas filament minus-ends could be bound to Arp2/3. The total numbers N_{tot} of actin monomers, N_{form} of formins, and N_{arp} of Arp2/3 complexes were fixed. We only considered Arp2/3 complexes as single entities and did not distinguish their subunits. Similarly, formins were assumed to be single molecules, ignoring their dimeric character. Diffusion of free G-actin monomers is assumed to be very fast such that the concentration of free monomers is homogeneous in the simulated volume. Monomers were added to free plus-ends at rate $k_{\text{on}} = r_{\text{on}} c_{\text{act}}^{\text{SS}}$, with $c_{\text{act}}^{\text{SS}}$ being the free monomer concentration at steady state and r_{on} being the actin polymerization rate. Filaments have been assumed to lose monomers from a free minus-end at rate k_{off} . The effective length added by a single monomer to a filament was 2.7 nm, corresponding to one-half of its radius. To mimic the finite persistence length of the filaments, we chose the orientation of a newly added monomer from a normal distribution with a variance of 0.02 and a mean equal to the orientation of the previous monomer. Free formins nucleated new filaments from a free monomer. The Arp2/3 complex was implemented as a minus-end capping protein that was able to nucleate new filaments while bound to the side of a mother filament. A filament having an Arp2/3 complex at its minus-end did not lose monomers from that end. An Arp2/3 complex was assumed to detach from the minus-end at rate $\omega_{\text{off,A}}$. Simulations were first run until the system reached steady state. After a time of the order of $T = 10^3$ s, the system was “bleached” by marking all monomers inside the filaments as nonfluorescent. Monomers that were subsequently incorporated into a filament were set to be fluorescent. The fluorescence within the bleached zone was then given by the number of fluorescent monomers that had been incorporated into the bleached filaments since the photobleaching pulse. The cortex was represented on a 2D grid of 200 pixels \times 200 pixels. On the camera, each pixel had a width of 133 nm such that the image showed a rectangular section of side length 26.6 μm . We chose periodic boundary conditions for our simulations to reflect the fact that the cell was manyfold larger than the bleached zone.

Calcium response measurements

Jurkat T cells were labeled with 4 μM Fluo-4 AM (F-14201, Invitrogen) for 30 min at room temperature with 2.5 mM probenecid (P-36400, Invitrogen) in RPMI (Sigma-Aldrich) without supplements. Cells were then washed in HEPES buffered saline (HBS; 51558, Sigma-Aldrich), and the medium was changed to HBS containing 2.5 mM probenecid before their addition to the microscope sample container with the prepared microscope coverslip. Cells were imaged at 37°C and 5% CO_2 using a 10 \times air objective on the spinning disc confocal microscope (Zeiss Cell Observer Spinning Disc Confocal), with 488-nm laser excitation and fluorescence detection around 530 nm and with an exposure time of 350 ms and a time between frames of 500 ms for 840 frames.

We used a custom-written analysis software, CalQuo (45), to detect single-cell landing events on the prepared coverslip surfaces and to record fluorescence intensities over time at the coverslip surface. For each cell, changes in fluorescence intensity above background levels (more than threefold) were indicative of the cell “landing” (slight increase) and calcium responses associated with Jurkat T cell signaling (strong, sharp increase). For each cell, CalQuo also determined the time lapse between “landing” and “signaling,” and it allowed for an accurate statistical, automated analysis of all individual cells over the

whole cell ensemble, resulting most importantly in the fraction of signaling cells.

The time-lapse trajectories of the Jurkat T cells dropping down, landing, and signaling on the coverslip surface were projected into one plane (fig. S7). Differences in fluorescence intensity were coded with cold (blue) to warm (red) colors representing low to high intensities. Practically, nonsignaling Jurkat T cells showed hardly any difference in fluorescence intensity over their trajectories and therefore were represented with cold colors, whereas Jurkat T cells releasing calcium turned red at the terminus of their tracks. For each experimental condition, we analyzed the calcium responses from at least 1500 individual cells over the course of at least three independent experiments.

Interference reflection microscopy

IRM experiments were performed at 37°C and 5% CO_2 with a 1.4 NA 63 \times oil immersion objective on a scanning laser confocal microscope (Zeiss 780, Carl Zeiss AG). IRM is a valuable technique for label-free, high-contrast, direct visualization of cell contacts at a glass interface. IRM is easily implemented on standard confocal microscopes provided that the configuration includes a neutral beam splitter that splits the excitation light such that destructive interference patterns are selectively created only at points where cell contacts with a glass interface occur. In our experiments, we used a 647-nm laser, a NT80/20 neutral beam splitter (20% excitation reflected, 80% emission transmitted), and a GaAsP detector operated in reflection mode. IRM images were recorded at a frame repetition of 6.2 s and simultaneously combined with fluorescence imaging of calcium responses using Fluo-4 (excited at 488 nm and detection around 530 nm) and with DIC imaging using the microscope’s TPMT (transmission photomultiplier tube) module for observation of the cell body.

The IRM and DIC image sequences were analyzed using ImageJ (<http://imagej.nih.gov/>) to manually determine the time points of Jurkat T cell landing (IRM), polarization (DIC), and contraction (IRM and DIC), whereas the calcium response was derived from a sharp increase in the fluorescence channel. Triggering times were calculated by comparison of the time points of landing and calcium release. Means and SDs were calculated following standard statistical principles. For each experimental condition, we analyzed the calcium and F-actin responses from at least 15 individual cells over the course of at least three independent experiments.

SUPPLEMENTARY MATERIALS

Supplementary material for this article is available at <http://advances.sciencemag.org/cgi/content/full/3/6/e1603032/DC1>

- fig. S1. Calibration of the STED microscope.
- fig. S2. Examples of the ramified actin network during active undulations and contractions of the lamellipodium in activated T cells.
- fig. S3. Exemplification of the basis of the actin meshwork analysis.
- fig. S4. Further details of LLSM imaging.
- fig. S5. Quantification of Jurkat T cell topology during activation on anti-CD3 ϵ - and anti-CD28-coated glass from the LLSM data.
- fig. S6. Correlation between actin and TCR reorganization in live Jurkat T cells after activation on anti-CD3 ϵ - and anti-CD28-coated glass.
- fig. S7. FCS analysis of G-actin diffusion in the cytoplasm of live Jurkat T cells for the different conditions.
- fig. S8. Representative data for determination of cortical actin filament lengths out of the FRAP data using computer simulations.
- fig. S9. Analysis of calcium response in the Jurkat T cells (signaling) using Fluo-4 for different conditions.
- fig. S10. LLSM time-lapse imaging of citrine-actin in live Jurkat T cells after making contact with anti-CD3 ϵ - and anti-CD28-coated glass and after treatment with 10 μM cytoD for 60 min.

table S1. Summary of average actin turnover half-times.

table S2. Summary of actin turnover rates.

movie S1. LLSM movie of membrane ruffling of a Jurkat T cell expressing lymphocyte-specific protein tyrosine kinase tagged with SNAP-Cell 505 on nonactivating glass.

movie S2. LLSM movie of Jurkat T cell activation in three steps.

movie S3. LLSM movie of lamellipod undulation of an activated Jurkat T cell.

movie S4. Confocal time-lapse movie of an activated Jurkat T cell.

movie S5. Confocal time-lapse movie of an activated Jurkat T cell.

movie S6. Spinning-disc microscopy time-lapse movie of suspended Jurkat T cells with Fluo-4 calcium indicator.

movie S7. Spinning-disc microscopy time-lapse movie of activated Jurkat T cells with Fluo-4 calcium indicator.

movie S8. Spinning-disc microscopy time-lapse of Jurkat T cells with Fluo-4 calcium indicator.

movie S9. Confocal time-lapse movie of an activated Jurkat T cell with Fluo-4 tagging.

movie S10. LLSM movie of cell wobbling of a Jurkat T cell.

movie S11. Spinning-disc microscopy time-lapse movie of Jurkat T cells.

REFERENCES AND NOTES

- M. Krause, A. S. Sechi, M. Konrad, D. Monner, F. B. Gertler, J. Wehland, Fyn-binding protein (Fyb)/SLP-76-associated protein (SLAP), Ena/vasodilator-stimulated phosphoprotein (VASP) proteins and the Arp2/3 complex link T cell receptor (TCR) signaling to the actin cytoskeleton. *J. Cell Biol.* **149**, 181–194 (2000).
- S. C. Bunnell, V. Kapoor, R. P. Triple, W. Zhang, L. E. Samelson, Dynamic actin polymerization drives T cell receptor-induced spreading: A role for the signal transduction adaptor LAT. *Immunity* **14**, 315–329 (2001).
- J. L. Cannon, J. K. Burkhardt, The regulation of actin remodeling during T-cell-APC conjugate formation. *Immunol. Rev.* **186**, 90–99 (2002).
- G. Campi, R. Varma, M. L. Dustin, Actin and agonist MHC-peptide complex-dependent T cell receptor microclusters as scaffolds for signaling. *J. Exp. Med.* **202**, 1031–1036 (2005).
- T. S. Gomez, K. Kumar, R. B. Medeiros, Y. Shimizu, P. J. Leibson, D. D. Billadeau, Formins regulate the actin-related protein 2/3 complex-independent polarization of the centrosome to the immunological synapse. *Immunity* **26**, 177–190 (2007).
- P. L. Schwartzberg, Formin the way. *Immunity* **26**, 139–141 (2007).
- D. D. Billadeau, J. C. Nolz, T. S. Gomez, Regulation of T-cell activation by the cytoskeleton. *Nat. Rev. Immunol.* **7**, 131–143 (2007).
- B. Reicher, M. Barda-Saad, Multiple pathways leading from the T-cell antigen receptor to the actin cytoskeleton network. *FEBS Lett.* **584**, 4858–4864 (2010).
- A. A. Smoligovets, A. W. Smith, H.-J. Wu, R. S. Petit, J. T. Groves, Characterization of dynamic actin associations with T-cell receptor microclusters in primary T cells. *J. Cell Sci.* **125**, 735–742 (2012).
- A. Babich, S. Li, R. S. O'Connor, M. C. Milone, B. D. Freedman, J. K. Burkhardt, F-actin polymerization and retrograde flow drive sustained PLC γ 1 signaling during T cell activation. *J. Cell Biol.* **197**, 775–787 (2012).
- Y. Yu, A. A. Smoligovets, J. T. Groves, Modulation of T cell signaling by the actin cytoskeleton. *J. Cell Sci.* **126**, 1049–1058 (2013).
- A. T. Ritter, Y. Asano, J. C. Stinchcombe, N. M. G. Dieckmann, B.-C. Chen, C. Gawden-Bone, S. van Engelenburg, W. Legant, L. Gao, M. W. Davidson, E. Betzig, J. Lippincott-Schwartz, G. M. Griffiths, Actin depletion initiates events leading to granule secretion at the immunological synapse. *Immunity* **42**, 864–876 (2015).
- S. C. Bunnell, D. I. Hong, J. R. Kardon, T. Yamazaki, C. J. McGlade, V. A. Barr, L. E. Samelson, T cell receptor ligation induces the formation of dynamically regulated signaling assemblies. *J. Cell Biol.* **158**, 1263–1275 (2002).
- M. Barda-Saad, A. Braiman, R. Tencer, S. C. Bunnell, V. A. Barr, L. E. Samelson, Dynamic molecular interactions linking the T cell antigen receptor to the actin cytoskeleton. *Nat. Immunol.* **6**, 80–89 (2005).
- M. Barda-Saad, N. Shirasu, M. H. Pauker, N. Hassan, O. Perl, A. Balbo, H. Yamaguchi, J. C. D. Houtman, E. Appella, P. Schuck, L. E. Samelson, Cooperative interactions at the SLP-76 complex are critical for actin polymerization. *EMBO J.* **29**, 2315–2328 (2010).
- A. C. N. Brown, S. Oddos, I. M. Dobbie, J.-M. Alakoskela, R. M. Parton, P. Eissmann, M. A. A. Neil, C. Dunsby, P. M. W. French, I. Davis, D. M. Davis, Remodelling of cortical actin where lytic granules dock at natural killer cell immune synapses revealed by super-resolution microscopy. *PLOS Biol.* **9**, e1001152 (2011).
- T. N. Sims, T. J. Soos, H. S. Xenias, B. Dubin-Thaler, J. M. Hofman, J. C. Waite, T. O. Cameron, V. K. Thomas, R. Varma, C. H. Wiggins, M. P. Sheetz, D. R. Littman, M. L. Dustin, Opposing effects of PKC θ and WASP on symmetry breaking and relocation of the immunological synapse. *Cell* **129**, 773–785 (2007).
- J. A. Theriot, The polymerization motor. *Traffic* **1**, 19–28 (2000).
- R. J. Pelham Jr., F. Chang, Actin dynamics in the contractile ring during cytokinesis in fission yeast. *Nature* **419**, 82–86 (2002).
- G. Salbreux, G. Charras, E. Paluch, Actin cortex mechanics and cellular morphogenesis. *Trends Cell Biol.* **22**, 536–545 (2012).
- M. Fritzsche, A. Lewalle, T. Duke, K. Kruse, G. Charras, Analysis of turnover dynamics of the submembranous actin cortex. *Mol. Biol. Cell* **24**, 757–767 (2013).
- M. Bovellan, Y. Romeo, M. Biro, A. Boden, P. Chugh, A. Yonis, M. Vaghela, M. Fritzsche, D. Moulding, R. Thorogate, A. Jégou, A. J. Thrasher, G. Romet-Lemonne, P. P. Roux, E. K. Paluch, G. Charras, Cellular control of cortical actin nucleation. *Curr. Biol.* **24**, 1628–1635 (2014).
- M. Fritzsche, C. Erlelkämper, E. Moeendarbary, G. Charras, K. Kruse, Actin kinetics shapes cortical network structure and mechanics. *Sci. Adv.* **2**, e1501337 (2016).
- A. Zumdieck, K. Kruse, H. Bringmann, A. A. Hyman, F. Jülicher, Stress generation and filament turnover during actin ring constriction. *PLOS ONE* **2**, e696 (2007).
- S. A. Koestler, A. Steffen, M. Nemethova, M. Winterhoff, N. Luo, J. M. Holleboom, J. Krupp, S. Jacob, M. Vinzenz, F. Schur, K. Schlüter, P. W. Gunning, C. Winkler, C. Schmeiser, J. Faix, T. E. B. Stradal, J. V. Small, K. Rottner, Arp2/3 complex is essential for actin network treadmilling as well as for targeting of capping protein and cofilin. *Mol. Biol. Cell* **24**, 2861–2875 (2013).
- J. K. Jun, A. H. Hubler, Formation and structure of ramified charge transportation networks in an electromechanical system. *Proc. Natl. Acad. Sci. U.S.A.* **102**, 536–540 (2005).
- R. Dominguez, K. C. Holmes, Actin structure and function. *Annu. Rev. Biophys.* **40**, 169–186 (2011).
- M. Murrell, P. W. Oakes, M. Lenz, M. L. Gardel, Forcing cells into shape: The mechanics of actomyosin contractility. *Nat. Rev. Mol. Cell Biol.* **16**, 486–498 (2015).
- M. Fritzsche, G. T. Charras, Dissecting protein reaction dynamics in living cells by fluorescence recovery after photobleaching. *Nat. Protoc.* **10**, 660–680 (2015).
- S. Kumari, D. Depoil, R. Martinelli, E. Judokosumo, G. Carmona, F. B. Gertler, L. C. Kam, C. V. Carman, J. K. Burkhardt, D. J. Irvine, M. L. Dustin, Actin foci facilitate activation of the phospholipase C- γ in primary T lymphocytes via the WASP pathway. *eLife* **4**, (2015).
- J. C. Stinchcombe, E. Majorovits, G. Bossi, S. Fuller, G. M. Griffiths, Centrosome polarization delivers secretory granules to the immunological synapse. *Nature* **443**, 462–465 (2006).
- R. Varma, G. Campi, T. Yokosuka, T. Saito, M. L. Dustin, T cell receptor-proximal signals are sustained in peripheral microclusters and terminated in the central supramolecular activation cluster. *Immunity* **25**, 117–127 (2006).
- T. Ilani, G. Vasiliver-Shamis, S. Vardhana, A. Bretscher, M. L. Dustin, T cell antigen receptor signaling and immunological synapse stability require myosin IIA. *Nat. Immunol.* **10**, 531–539 (2009).
- P. Beemiller, M. F. Krummel, Mediation of T-cell activation by actin meshworks. *Cold Spring Harb. Perspect. Biol.* **2**, a002444 (2010).
- J. A. Hammer III, J. K. Burkhardt, Controversy and consensus regarding myosin II function at the immunological synapse. *Curr. Opin. Immunol.* **25**, 300–306 (2013).
- M. L. Dustin, The immunological synapse. *Cancer Immunol. Res.* **2**, 1023–1033 (2014).
- G. W. Ashdown, A. Cope, P. W. Wiseman, D. M. Owen, Molecular flow quantified beyond the diffraction limit by spatiotemporal image correlation of structured illumination microscopy data. *Biophys. J.* **107**, L21–L23 (2014).
- S. Murgesan, J. Hong, J. Yi, D. Li, J. R. Beach, L. Shao, J. Meinhardt, G. Madison, X. Wu, E. Betzig, J. A. Hammer, Formin-generated actomyosin arcs propel T cell receptor microcluster movement at the immune synapse. *J. Cell Biol.* **215**, 383–399 (2016).
- M. Huse, L. O. Klein, A. T. Girvin, J. M. Faraj, Q. J. Li, M. S. Kuhns, M. M. Davis, Spatial and temporal dynamics of T cell receptor signaling with a photoactivatable agonist. *Immunity* **27**, 76–88 (2007).
- A. D. Douglass, R. D. Vale, Single-molecule microscopy reveals plasma membrane microdomains created by protein-protein networks that exclude or trap signaling molecules in T cells. *Cell* **17**, 937–950 (2005).
- B. F. Lillemeier, M. A. Mörtelmaier, M. B. Forstner, J. B. Huppa, J. T. Groves, M. M. Davis, TCR and Lat are expressed on separate protein islands on T cell membranes and concatenate during activation. *Nat. Immunol.* **11**, 90–96 (2010).
- J. Rossy, D. M. Owen, D. J. Williamson, Z. Yang, K. Gaus, Conformational states of the kinase Lck regulate clustering in early T cell signaling. *Nat. Immunol.* **14**, 82–89 (2013).
- S. Kumari, S. Curado, V. Mayya, M. L. Dustin, T cell antigen receptor activation and actin cytoskeleton remodeling. *Biochim. Biophys. Acta* **1838**, 546–556 (2014).
- B.-C. Chen, W. R. Legant, K. Wang, L. Shao, D. E. Milkie, M. W. Davidson, C. Janetopoulos, X. S. Wu, J. A. Hammer, Z. Liu, B. P. English, Y. Mimori-Kiyosue, D. P. Romero, A. T. Ritter, J. Lippincott-Schwartz, L. Fritz-Laylin, R. D. Mullins, D. M. Mitchell, J. N. Bembek, A.-C. Reymann, R. Böhme, S. W. Grill, J. T. Wang, G. Seydoux, U. S. Tulu, D. P. Kiehart, E. Betzig, Lattice light-sheet microscopy: Imaging molecules to embryos at high spatiotemporal resolution. *Science* **346**, 1257998 (2014).
- M. Fritzsche, R. A. Fernandes, H. Colin-York, A. M. Santos, S. F. Lee, B. C. Lagerholm, S. J. Davis, C. Eggeling, CalQuo: Automated, simultaneous single-cell and population-level quantification of intracellular Ca²⁺ responses. *Sci. Rep.* **5**, 16487 (2015).

46. K. Xu, H. P. Babcock, X. Zhuang, Dual-objective STORM reveals three-dimensional filament organization in the actin cytoskeleton. *Nat. Methods* **9**, 185–188 (2012).
47. Y. Kaizuka, A. D. Douglass, R. Varma, M. L. Dustin, R. D. Vale, Mechanisms for segregating T cell receptor and adhesion molecules during immunological synapse formation in Jurkat T cells. *Proc. Natl. Acad. Sci. U.S.A.* **104**, 20296–20301 (2007).
48. O. Dushek, S. Mueller, S. Soubies, D. Depoil, I. Caramalho, D. Coombs, S. Valitutti, Effects of intracellular calcium and actin cytoskeleton on TCR mobility measured by fluorescence recovery. *PLOS ONE* **3**, e3913 (2008).
49. A. L. DeMond, K. D. Mossman, T. Starr, M. L. Dustin, J. T. Groves, T cell receptor microcluster transport through molecular mazes reveals mechanism of translocation. *Biophys. J.* **94**, 3286–3292 (2008).
50. A. J. Ridley, M. A. Schwartz, K. Burridge, R. A. Firtel, M. H. Ginsberg, G. Borisy, J. T. Parsons, A. R. Horwitz, Cell migration: Integrating signals from front to back. *Science* **302**, 1704–1709 (2003).
51. T. Yokosuka, K. Sakata-Sogawa, W. Kobayashi, M. Hiroshima, A. Hashimoto-Tane, M. Tokunaga, M. L. Dustin, T. Saito, Newly generated T cell receptor microclusters initiate and sustain T cell activation by recruitment of Zap70 and SLP-76. *Nat. Immunol.* **6**, 1253–1262 (2005).
52. J. Yi, X. S. Wu, T. Crites, J. A. Hammer III, Actin retrograde flow and actomyosin II arc contraction drive receptor cluster dynamics at the immunological synapse in Jurkat T cells. *Mol. Biol. Cell* **23**, 834–852 (2012).
53. H.-G. Döbereiner, B. J. Dubin-Thaler, J. M. Hofman, H. S. Xenias, T. N. Sims, G. Giannone, M. L. Dustin, C. H. Wiggins, M. P. Sheetz, Lateral membrane waves constitute a universal dynamic pattern of motile cells. *Phys. Rev. Lett.* **97**, 038102 (2006).
54. L. Blanchoin, R. Boujemaa-Paterski, C. Sykes, J. Plastino, Actin dynamics, architecture, and mechanics in cell motility. *Physiol. Rev.* **94**, 235–263 (2014).
55. D. Malinova, M. Fritzsche, C. R. Nowosad, H. Armer, P. M. G. Munro, M. P. Blundell, G. Charras, P. Tolar, G. Bouma, A. J. Thrasher, WASp-dependent actin cytoskeleton stability at the dendritic cell immunological synapse is required for extensive, functional T cell contacts. *J. Leukoc. Biol.* **99**, 699–710 (2016).
56. M. Bai, A. R. Missel, A. J. Levine, W. S. Klug, On the role of the filament length distribution in the mechanics of semiflexible networks. *Acta Biomater.* **7**, 2109–2118 (2011).
57. E. Judokusumo, E. Tabdanov, S. Kumari, M. L. Dustin, L. C. Kam, Mechanosensing in T lymphocyte activation. *Biophys. J.* **102**, L5–L7 (2012).
58. E. Tabdanov, S. Gondarenko, S. Kumari, A. Liapis, M. L. Dustin, M. P. Sheetz, L. C. Kam, T. Iskratsch, Micropatterning of TCR and LFA-1 ligands reveals complementary effects on cytoskeleton mechanics in T cells. *Integr. Biol.* **7**, 1272–1284 (2015).
59. R. Basu, B. M. Whitlock, J. Husson, A. Le Floch, W. Jin, A. Oyler-Yaniv, F. Dotiwala, G. Giannone, C. Hivroz, N. Biais, J. Lieberman, L. C. Kam, M. Huse, Cytotoxic T cells use mechanical force to potentiate target cell killing. *Cell* **165**, 100–110 (2016).
60. H. Colin-York, D. Shrestha, J. H. Felce, D. Waithe, E. Moeendarbary, S. J. Davis, C. Eggeling, M. Fritzsche, Super-resolved traction force microscopy (STFM). *Nano Lett.* **16**, 2633–2638 (2016).
61. V. T. Chang, R. A. Fernandes, K. A. Ganzinger, S. F. Lee, C. Siebold, J. McColl, P. Jönsson, M. Palayret, K. Harlos, C. H. Coles, E. Y. Jones, Y. Lui, E. Huang, R. J. C. Gilbert, D. Klennerman, A. R. Aricescu, S. J. Davis, Initiation of T cell signaling by CD45 segregation at ‘close contacts’. *Nat. Immunol.* **17**, 574–582 (2016).
62. N. J. Burroughs, Z. Lazic, P. A. van der Merwe, Ligand detection and discrimination by spatial relocation: A kinase-phosphatase segregation model of TCR activation. *Biophys. J.* **91**, 1619–1629 (2006).

Acknowledgments: We thank H. White for technical support, along with L. D. Lavis for their gifts of reagents. **Funding:** We thank the Wolfson Imaging Centre–Oxford for providing microscope facility support, the Wolfson Foundation, the Medical Research Council (MRC) (grant number MC_UU_12010/unit programs G0902418 and MC_UU_12025), the MRC/Biotechnology and Biological Sciences Research Council (BBSRC)/Engineering and Physical Sciences Research Council (EPSRC) (grant number MR/K01577X/1), and the Wellcome Trust (grant 104924/14/Z/14) for microscope funding and for funding M.F., R.A.F., D.W., B.C.L., J.B.d.I.S., S.J.D., and C. Eggeling. H.C. was funded by the EPSRC, and S.J.D. was funded by the Wellcome Trust. M.P.C. was funded by the Alfred Benzon Foundation. We thank the Company of Biologists for the travel grant awarded to M.F. J.B.d.I.S. acknowledges funding by the Marie Curie Career Integration Grant. **Author contributions:** M.F. and C. Eggeling developed the concept and designed the experimental approach. M.F., V.T.C., H.C.-Y., M.P.C., J.H.F., S.G., C. Erenkämper, J.M.H., and I.P.-P. carried out the experiments and implemented the data analysis. M.F., C. Eggeling, S.J.D., and E.B. wrote the article. All other authors provided samples, performed experiments, and helped with experimental setups. All were involved in discussion of data and manuscript editing. **Competing interests:** Lattice light sheet microscopy is covered by the following patents: U.S. Patent 7,894,136 issued to E.B. and assigned to Lattice Light, LLC of Ashburn, VA; U.S. Patents 8,711,211, 9,223,125, 9,448,395, and 9,477,074 issued to E.B. and assigned to Howard Hughes Medical Institute (HHMI); and U.S. Patent applications 13/844,405, 14/215,976, and 14/216,015 filed by E.B. and assigned to HHMI. All other authors declare that they have no competing interests. **Data and materials availability:** All data needed to evaluate the conclusions in the paper are present in the paper and/or the Supplementary Materials. Additional data related to this paper may be requested from the authors.

Submitted 8 December 2016

Accepted 27 April 2017

Published 21 June 2017

10.1126/sciadv.1603032

Citation: M. Fritzsche, R. A. Fernandes, V. T. Chang, H. Colin-York, M. P. Clausen, J. H. Felce, S. Galiani, C. Erenkämper, A. M. Santos, J. M. Heddleston, I. Pedroza-Pacheco, D. Waithe, J. B. de la Serna, B. C. Lagerholm, T.-I. Liu, T.-L. Chew, E. Betzig, S. J. Davis, C. Eggeling, Cytoskeletal actin dynamics shape a ramifying actin network underpinning immunological synapse formation. *Sci. Adv.* **3**, e1603032 (2017).

Cytoskeletal actin dynamics shape a ramifying actin network underpinning immunological synapse formation

Marco Fritzsche, Ricardo A. Fernandes, Veronica T. Chang, Huw Colin-York, Mathias P. Clausen, James H. Felce, Silvia Galiani, Christoph Erlenkämper, Ana M. Santos, John M. Heddleston, Isabela Pedroza-Pacheco, Dominic Waithe, Jorge Bernardino de la Serna, B. Christoffer Lagerholm, Tsung-li Liu, Teng-Leong Chew, Eric Betzig, Simon J. Davis and Christian Eggeling

Sci Adv **3** (6), e1603032.
DOI: 10.1126/sciadv.1603032

ARTICLE TOOLS

<http://advances.sciencemag.org/content/3/6/e1603032>

SUPPLEMENTARY MATERIALS

<http://advances.sciencemag.org/content/suppl/2017/06/19/3.6.e1603032.DC1>

REFERENCES

This article cites 61 articles, 20 of which you can access for free
<http://advances.sciencemag.org/content/3/6/e1603032#BIBL>

PERMISSIONS

<http://www.sciencemag.org/help/reprints-and-permissions>

Use of this article is subject to the [Terms of Service](#)

Science Advances (ISSN 2375-2548) is published by the American Association for the Advancement of Science, 1200 New York Avenue NW, Washington, DC 20005. 2017 © The Authors, some rights reserved; exclusive licensee American Association for the Advancement of Science. No claim to original U.S. Government Works. The title *Science Advances* is a registered trademark of AAAS.